Effects of fluid rheology on dynamics of a capsule through a microchannel constriction

Jingtao Ma,[1,2] Qiuxiang Huang,[3] Yi Zhu,[4] Yuan-Qing Xu,[5,a)] and Fang-Bao Tian[2]

AFFILIATIONS

[1]Aix Marseille Univ., CNRS, Centrale Marseille, M2P2, Marseille, France
[2]School of Engineering and Information Technology, University of New South Wales, Canberra, ACT 2600, Australia
[3]School of Mechanical, Medical and Process Engineering, Queensland University of Technology, Brisbane 4000, Australia
[4]Ocean Intelligence Technology Center, Shenzhen Institute of Guangdong Ocean University, Shenzhen, Guangdong 518055, China
[5]School of Medical Technology, Beijing Institute of Technology, Zhongguancun South Street, Beijing 100081, China

[a)]Author to whom correspondence should be addressed: bitxyq@bit.edu.cn

ABSTRACT

This paper numerically investigates the impact of fluid rheology on the behaviors of a spherical capsule through a microchannel constriction. Different flow scenarios are considered: a Newtonian capsule in a viscoelastic matrix, a Newtonian capsule in a Newtonian matrix, and a viscoelastic capsule in a Newtonian matrix. The results demonstrate that the capsule's lengths undergo oscillations during the passage through the constriction, with three stages of evolution. When approaching the constriction, the capsule respectively experiences increase and decrease in its length and height. While within or exiting the constriction, the length of the capsule continuously decreases, and the height generally increases. As the capsule moves away from the constriction, the capsule relaxes to different profiles in different flows. Detailed analysis on the effects of the fluid viscoelasticity on the capsule's lengths in different stages is provided. In addition, the behaviors of a red blood cell passing through a microchannel constriction are also examined. This study sheds light on the complex behaviors of a spherical capsule and red blood cell in microchannel constriction, emphasizing the significant influence of fluid rheology on their deformation and shape changes.

I. INTRODUCTION

A capsule refers to a flexible object consisting of a thin membrane that encloses a liquid core within it. The behaviors of capsules have garnered increasing interest owing to their significant role in various biomedical and industrial applications. For instance, lipid membrane-based carriers have been employed to transport drugs and vaccines, even those that may be harmful to the human body.[1–3]

Great efforts have been devoted to experimental and numerical investigations aimed at understanding the behavior of capsules in various flow conditions (e.g., shear flow[4–6] and channel flow[7–9]) In recent years, particular interest have been placed on the study of deformation and motion of elastic capsules through microchannel constrictions. This research is motivated by its relevance to understanding the behavior of cells in vessels with stenosis,[10] as well as, applications on manipulation of cells in microfluidics.[11] Previous experimental studies have mainly focused on measuring cell properties and manipulating cells (e.g., cell sorting[12,13]) For instance, Luo and colleagues[14] developed a microfluidic system incorporating a constriction to measure the Young's modulus of a cell. Their findings revealed a direct relationship between the Young's modulus of a cell and its length during passage through the constriction. Additionally, contraction-expansion structures in microchannels have been employed to effectively separate cancer cells from whole human blood, resulting in a remarkably high separation rate.[13]

Numerical simulations have also been conducted to investigate the behavior of cells passing through constrictions in microchannels. For example, Kusters *et al.*[15] numerically investigated the forced transport of an elastic particle through a narrow constriction and found that whether the particle blocks or passes through the constriction depends on both the size and length of the constriction segment. Park and Dimitrakopoulos[16] studied the effects of blockage ratio and viscosity ratio on the deformation of a capsule through a microchannel constriction. Their findings showed that the size of the capsule significantly affects the transition time and pressure drop through the constriction, while the viscosity ratio has only a weak effect. In addition, Lu and Peng[17] examined the deformation of a red blood cell

passing through an extremely narrow (sub micrometer) constriction. Their study reported that a higher pressure drop results in higher passing velocity and larger deformation, while the viscosity ratio does not significantly affect the transition time and deformation of the capsule.

The aforementioned investigations have provided valuable insights into the diverse behaviors of a capsule as it passes through a constriction segment in a microchannel. However, these studies have predominantly focused on Newtonian flows, neglecting the influence of fluid rheology on the capsule's behavior within constrictions. It is worth noting that many fluids encountered in biological systems and microfluidics exhibit non-Newtonian characteristics. For instance, human blood plasma has been documented to demonstrate robust viscoelastic characteristics.[18,19] Furthermore, viscoelastic behavior has also been identified in the intracellular liquid (cell cytoplasm).[20,21] The presence of these internal and external viscoelastic fluids may significantly impact the behavior of a capsule in confined flows. In this study, we aim to investigate the influence of fluid viscoelasticity on the dynamic behaviors of a capsule through a microchannel constriction.

The organization of the rest of this paper is as follows: The problem statement, the mathematical models and the numerical methods utilized in the present work are introduced in Sec. II. In Sec. III, the results and discussion are presented. Final conclusions are provided in Sec. IV.

II. PROBLEM STATEMENT AND NUMERICAL METHODS

A. Problem statement

In this study, we investigate the dynamics of an initially spherical capsule flowing through a microchannel with a constriction segment. The geometric configuration of the microchannel is depicted in Fig. 1. The channel has a length of $20H_c$, where H_c represents the height of the constriction segment. In addition, the microchannel has a square cross-section with a side length of $4H_c$. The origin is positioned at the center of the microchannel. Consequently, the computational domain spans over $[-10H_c, 10H_c] \times [-2H_c, 2H_c] \times [-2H_c, 2H_c]$ along the x-, y-, and z-axis directions, while the constriction segments are located at $[-2H_c,2H_c]\times[-2H_c,2H_c]\times[H_c,2H_c]$ and $[-2H_c,2H_c]\times[-2H_c,2H_c]\times[-2H_c,-H_c]$.

An initially spherical capsule, with a radius of R, is positioned at the center of the microchannel's cross-section with $x = -4H_c$. The fluids both inside and outside the capsule can be either Newtonian or viscoelastic. To investigate the influence of fluid viscoelasticity on transient capsule behaviors, three distinct cases are simulated: a Newtonian capsule in a Newtonian matrix (N/N flow) as the baseline, a viscoelastic capsule in a Newtonian matrix (V/N flow), and a Newtonian capsule in a viscoelastic matrix (N/V flow). The viscoelastic properties of the fluid are modeled using the FENE-CR constitutive equation, which is commonly employed to model Boger fluids.[22] The FENE-CR model is utilized wherever the fluid exhibits viscoelasticity, while the Newtonian constitutive model is used elsewhere. The different fluids (internal and external fluids) are separated by the capsule

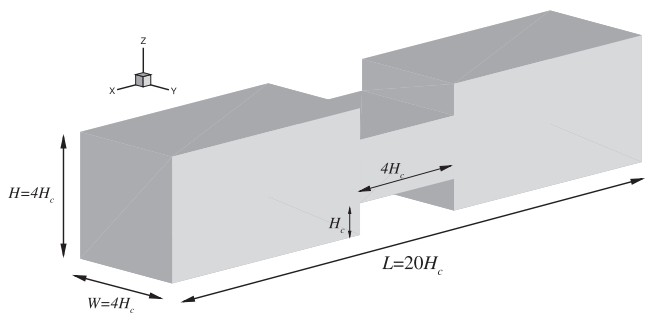

FIG. 1. Geometry of the microchannel with a constriction segment.

TABLE I. Non-dimensional parameters.

Name	Definition	Value
Reynolds number	$Re = \rho_f U_c W/\mu_0^{out}$	0.5
Weissenberg number	$Wi = \lambda_p \dot{\gamma}_{eff}$	0–100
The ratio of the internal to the external total viscosity	$\xi_\mu = \mu_0^{in}/\mu_0^{out}$	0.2–5.0
The ratio of the solvent to the total viscosity	$\beta = \mu_s/\mu_0$	0.5, 1.0
Capillary number	$Ca = \mu_0^{out} U_c/E_s$	0.0333
The non-dimensional bending stiffness	$e_b = E_b/E_s R^2$	0.001
Blockage ratio	$Br = 2R/2H_c$	1.0
The non-dimensional diffusion parameter	$Pr = \kappa/(U_c W)$	5.0×10^{-3}

TABLE II. Simulation parameters.

Name	Symbol	Value
Fluid density (kg/m^{-3})	ρ	1000
Channel width (μm)	W	40
Average inflow velocity (m/s)	U_c	0.0125–0.025
Solvent viscosity of external fluid (Pa s)	μ_s^{out}	1×10^3
Polymer viscosity of external fluid (Pa s)	μ_s^{out}	$0–1 \times 10^3$
Zero-shear viscosity of external fluid (Pa s)	μ_0^{out}	1×10^3–2×10^3
Solvent viscosity of internal fluid (Pa s)	μ_s^{in}	0.1×10^3–10×10^3
Polymer viscosity of internal fluid (Pa s)	μ_s^{in}	$0–5 \times 10^3$
Zero-shear viscosity of internal fluid (Pa s)	μ_0^{in}	0.2×10^3–10×10^3
Polymer extensibility parameter for FENE-CR model	L_p^2	$10^{-2} - 10^{10}$
Capsule radius (μm)	R	10
Capsule stretching modulus (N/m)	E_s	3.75×10^{-4}–1.5×10^{-3}
Capsule bending modulus (N m)	E_b	3.75×10^{-17}–1.5×10^{-16}

membrane, and to identify different fluids, the front-tracking method is employed. Detailed descriptions of the FENE-CR model and the front tracking method can be found below.

The membrane of the 3D capsule is a closed elastic surface with zero-thickness. The internal stretching and bending forces can be induced by the deformation of the membrane, and they can obtained by

$$\boldsymbol{f}_e + \boldsymbol{f}_b = -\frac{\delta(W^S + W^B)}{\delta \mathbf{X}}, \tag{1}$$

where $\mathbf{X}$ is the position of a node on the capsule membrane, $\boldsymbol{f}_e$ and $\boldsymbol{f}_b$ are, respectively, the internal elastic and bending forces induced by the deformation of the membrane, and W^S and W^B are total strain and bending energies.

For the bending energy, one of the most extensively used models, the Helfrich energy model, is employed, and it is given as[23,24]

$$W^B = \frac{E_b}{2}\int_A (2H - c_0)^2 dA, \tag{2}$$

where E_b is the bending rigidity, H is the mean curvature, and $c_0 = 0$ is the spontaneous curvature.

For the membrane strain energy, two models are considered here: the neo-Hookean law[25,26] (strain-softening) and the Skalak's (SK) law[27] (strain-hardening). For the neo-Hookean (NH) law which was originally used to model the volume-incompressible rubber-like materials, the strain energy takes the form of[25,26]

$$W^S = \int_A \frac{E_s}{6}\left(I_1 + \frac{1}{I_2 + 1} - 1\right) dA, \tag{3}$$

where A is the surface area, E_s is the stretching modulus, and I_1 and I_2 are the strain invariants of the surface deformation, obtained with the principal in-plane stretch ratios λ_1 and λ_2 according to

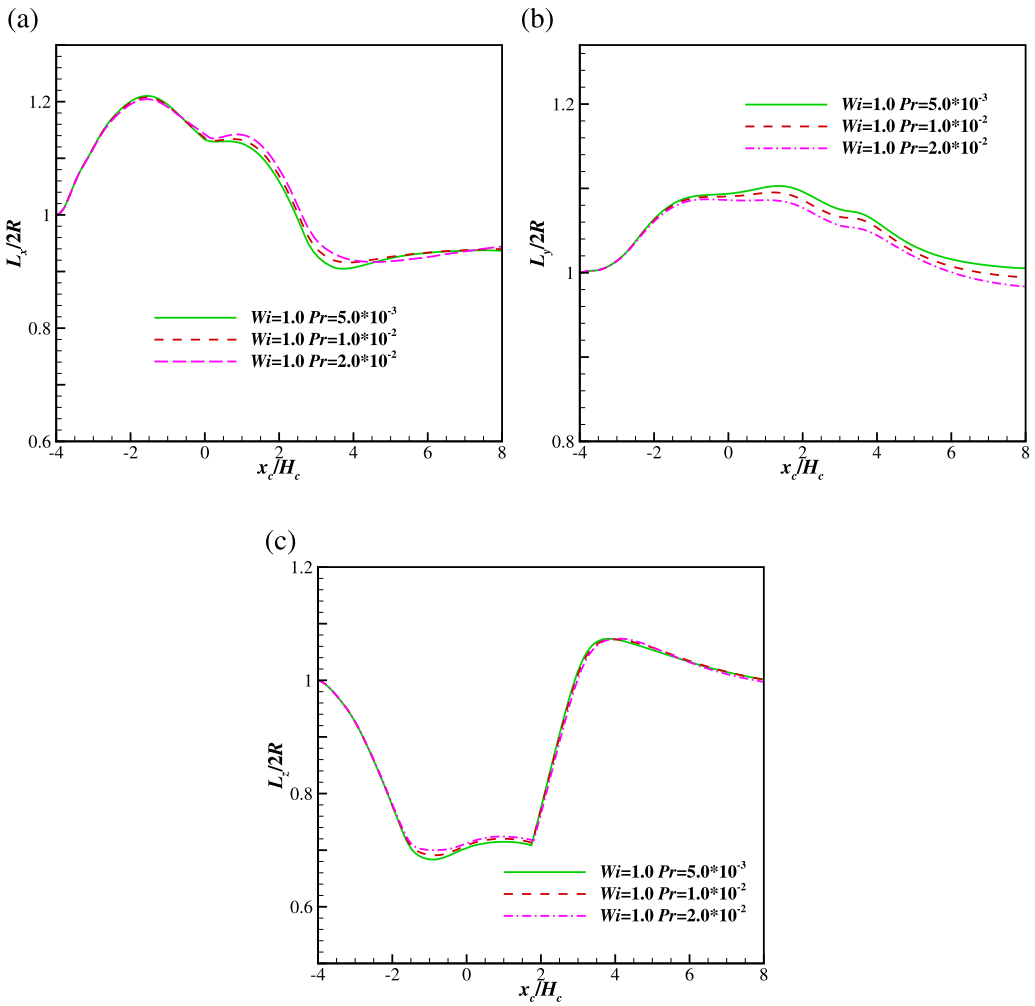

FIG. 2. The evolution of the lengths of the capsule as a function of the position of the capsule center x_c at $\xi_\mu = 1$ and $L_p^2 = 10^3$, $Wi = 1.0$ and different Pr in the N/V flow. (a) Length L_x, (b) width L_y, and height (c) L_z (scaled by the initial diameter of the capsule $2R$).

$$I_1 = \lambda_1^2 + \lambda_2^2 - 2, \tag{4}$$

$$I_2 = (\lambda_1 \lambda_2)^2 - 1. \tag{5}$$

For the Skalak's (SK) law, the strain energy function due to the stretching deformation is given by

$$W^S = \int_A \left[\frac{E_s}{12} \left(I_1^2 + 2I_1 - 2I_2 \right) + \frac{E_a}{12} I_2^2 \right] dA, \tag{6}$$

where E_a is elastic modulus for surface-area conservation. In the present study, the SK law with $C = E_a/E_s = 1$ is used to model the capsule membrane.

The fully developed laminar channel flow is applied at the inlet of the channel, and Neumann boundary conditions are set at the outlet. The non-slip boundary condition is imposed at the channel walls. The flows of the fluid are described by the continuity and Navier–Stokes equations[28,29]

$$\nabla \cdot \boldsymbol{u} = 0, \tag{7}$$

$$\frac{\partial(\rho \boldsymbol{u})}{\partial t} + \nabla \cdot (\rho \boldsymbol{u}\boldsymbol{u}) = \nabla \cdot (-p\boldsymbol{I} + 2\mu_s \boldsymbol{D} + \boldsymbol{\tau_p}), \tag{8}$$

where ρ is the fluid density, $\boldsymbol{u}$ is the velocity of the fluid, p is the pressure, μ_s is the solvent dynamic viscosity, $\boldsymbol{I}$ is the identity tensor, $\boldsymbol{D} = \frac{1}{2}[\nabla \boldsymbol{u} + (\nabla \boldsymbol{u})^T]$ is the strain rate tensor, and $\boldsymbol{\tau_p}$ is the viscoelastic stress tensor induced by the polymers in the solvent. In this work, the FENE-CR model is utilized to determine the viscoelastic stress $\boldsymbol{\tau_p}$ in terms of the conformation tensor $\boldsymbol{C}$ as,[28,30–32]

$$\boldsymbol{\tau_p} = \frac{\mu_p}{\lambda_p} F(\boldsymbol{C})(\boldsymbol{C} - \boldsymbol{I}) \quad (\text{FENE} - \text{CR}), \tag{9}$$

where μ_p and λ_p are, respectively, the dynamic viscosity and relaxation time of the polymer, and $F(\boldsymbol{C}) = \frac{1}{1 - tr(\boldsymbol{C})/L_p^2}$ is the spring function with L_p being the maximum extension length of the spring and tr($\boldsymbol{C}$) being

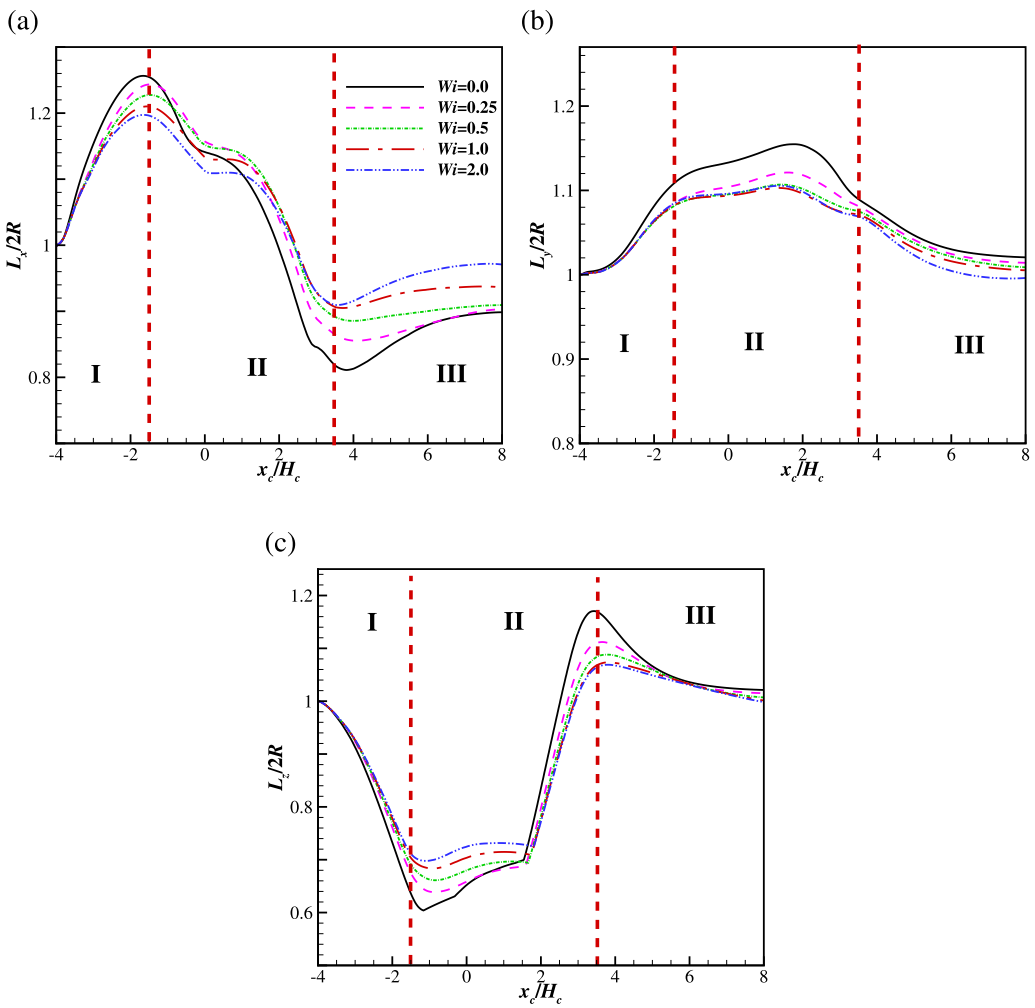

FIG. 3. The evolution of the lengths of the capsule as a function of the position of the capsule center x_c at $\xi_\mu = 1$ and $L_p^2 = 10^3$ and different *Wi* in the N/V flow. (a) Length L_x, (b) width L_y, and height (c) L_z (scaled by the initial diameter of the capsule $2R$).

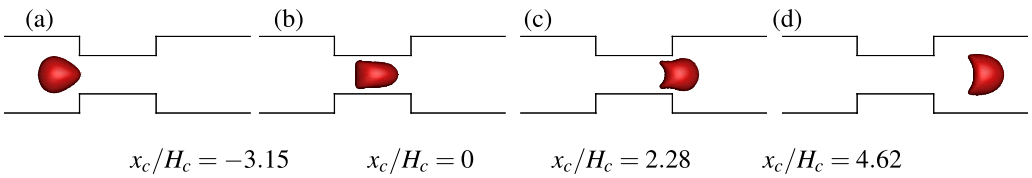

FIG. 4. The instantaneous profiles of the capsule at $Wi = 2.0$ at different positions: (a) $x_c/H_c = -3.15$, (b) $x_c/H_c = 0$, (c) $x_c/H_c = 2.28$ and (d) $x_c/H_c = 4.62$.

the trace of the tensor $\boldsymbol{C}$. The conformation tensor $\boldsymbol{C}$ is computed by the following transport equations,

$$\frac{\partial \boldsymbol{C}}{\partial t} + (\boldsymbol{u}\cdot\nabla)\boldsymbol{C} = -\frac{F(\boldsymbol{C})}{\lambda_p}(\boldsymbol{C}-\boldsymbol{I}) + \boldsymbol{C}\cdot\nabla\boldsymbol{u} + (\nabla\boldsymbol{u})^T\cdot\boldsymbol{C} \quad (\text{FENE}-\text{CR}). \tag{10}$$

To simulate multiphase flows, we employ the front-tracking method.[33,34] Following the treatment used in Luo *et al.*,[35] the multiphase problem is treated as one-phase flow, with the sharp material property (i.e., solvent viscosity μ_s, polymer viscosity μ_p, and polymer relaxation time λ_p) variations across the capsule membrane. In this case, the flows inside and outside the capsule can be simultaneously obtained on a stationary Eulerian grid through the solution of a single set of governing equations [i.e., Eqs. (7) and (8)] across the entire computational domain. It should be noted that the constitutive equations [i.e., Eqs. (9) and (10)] for the viscoelastic stress $\boldsymbol{\tau_p}$ is also solved over the whole domain, while $\mu_p = 0$ and $\lambda_p = 0$ are utilized for the Newtonian phase.

Within the front-tracking method, the material properties of the fluid, including the solvent viscosity μ_s, polymer viscosity μ_p, and polymer relaxation time λ_p, at a grid node $\boldsymbol{x}$ are computed as follows:

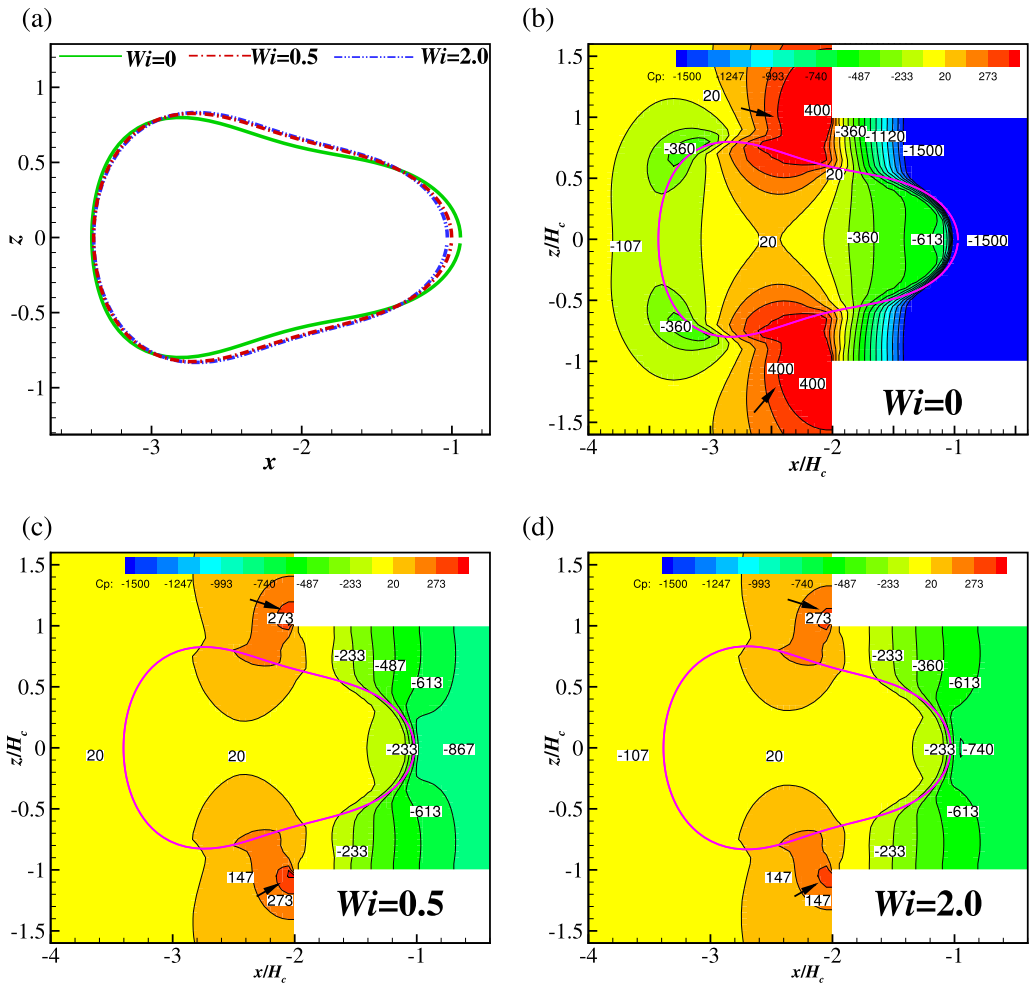

FIG. 5. (a) The instantaneous profiles of the capsule in plane $y = 0$ at $x_c/H_c = -2.336$ and different Wi. (b)-(d) The distributions of the pressure coefficient C_p at different Wi.

$$\psi(\boldsymbol{x}) = \psi^{\text{out}} + \left(\psi^{\text{in}} - \psi^{\text{out}}\right) I(\boldsymbol{x}), \tag{11}$$

where ψ represents the material properties of the fluid, of which the values inside and outside the capsule are denoted by the superscripts "in" and "out," respectively, and the indicator function $I(\boldsymbol{x})$ takes a value of 1 inside the capsule and 0 outside the capsule.

The non-dimensional parameters involved in this problem are: the Reynolds number $Re = \rho_f U_c W/\mu_0^{out}$, the Weissenberg number $Wi = \lambda_p \dot{\gamma}_{eff}$, the non-dimensional diffusion parameter $Pr = \kappa/(U_c W)$, the ratio of the internal to the external total viscosity $\xi_\mu = \mu_0^{in}/\mu_0^{out}$ the ratio of the solvent to the total viscosity $\beta = \mu_s/\mu_0$, the polymer extensibility parameter L_p^2, the capillary number $Ca = \mu_0^{out} U_c/E_s$, the non-dimensional bending stiffness $e_b = E_b/E_s R^2$, and the blockage ratio at the constriction segment $Br = 2R/2H_c$, where ρ_f is the fluid density, U_c is the mean velocity of the flow applied at the channel inlet, $\dot{\gamma}_{eff} = 2U_c/W$ is the effective wall shear rate, κ is the diffusion parameter, E_s and E_b are, respectively, the stretching and bending modulus of the capsule membrane, and $\mu_0^{in} = \mu_s^{in} + \mu_p^{in}$ and $\mu_0^{out} = \mu_s^{out} + \mu_p^{out}$ are, respectively, the total viscosities of the internal and external fluids of the capsule, with μ_s^{in} and μ_p^{in}, respectively, being the solvent and polymer viscosities of the internal fluid and μ_s^{out} and μ_p^{out}, respectively, being the solvent and polymer viscosities of the external fluid. The non-dimensional parameters involved in the present study is summarized in Table I. In addition, the real physical parameters involved in this study are listed in Table II for possible future comparison with experiments. It should be noted that the diffusion parameter κ is a parameter involved in the lattice Boltzmann method for viscoelastic constitutive equations [Eq. (10)], and details about this parameter can be found in our previous papers.[28,32] The grid spacing $\Delta x = \Delta y = \Delta z = R/20$ is used in all simulations, and validations have confirmed the mesh independence has been achieved at this grid spacing.

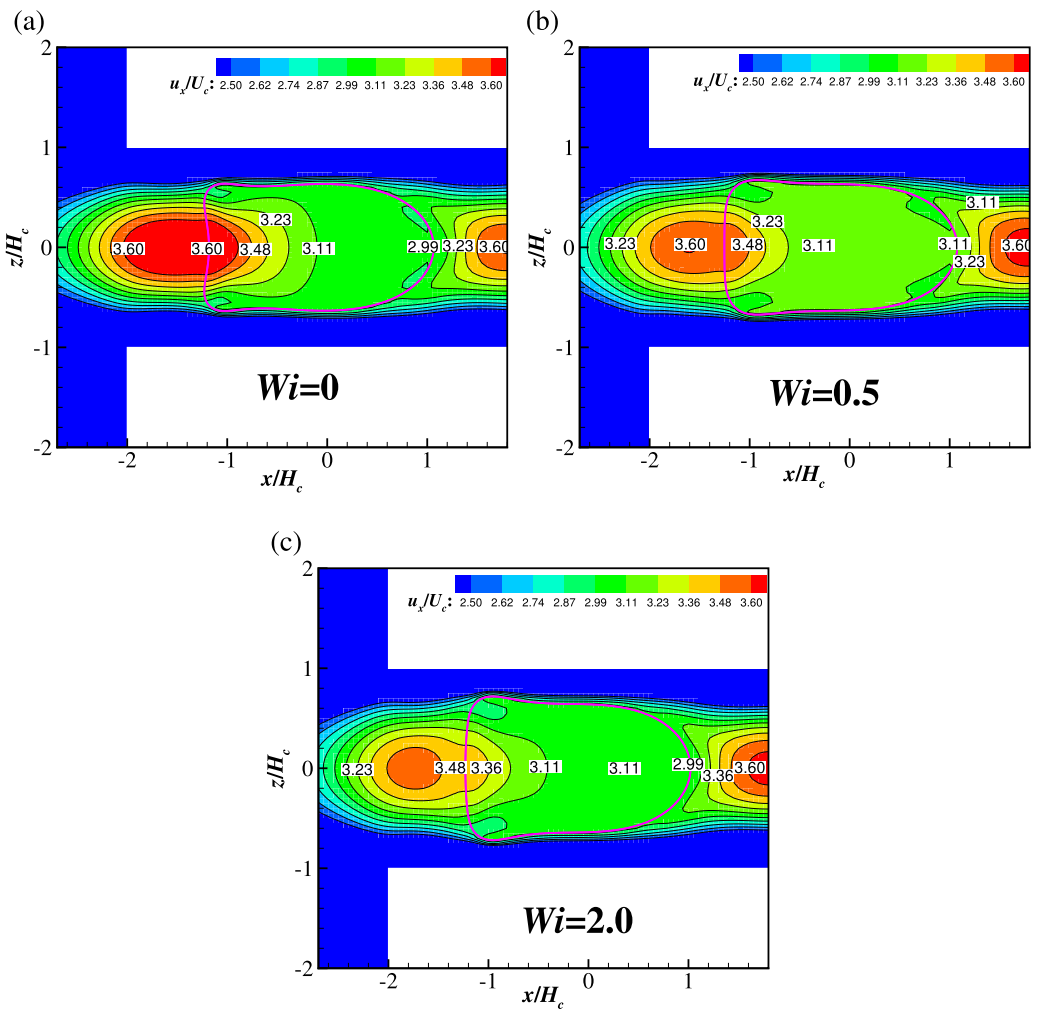

FIG. 6. The distributions of the flowing velocity in $x-$ axis direction (u_x) at $x_c/H_c = -0.226$ and Wi = (a) 0, (b) 0.5 and (c) 2.0.

B. Numerical method

In this study, the continuity and Navier–Stokes equations [Eqs. (7) and (8)], along with the constitutive equations for the FENE-CR fluid [Eq. (10)], are solved using the lattice Boltzmann method. Further details regarding the numerical method can be found in our previous papers.[4,28,32,36–39]

Within the frame of the front-tracking method, it is necessary to update the indicator function $I(\boldsymbol{x})$ at each time step. This is achieved by solving the following Poisson equation[33,34]

$$\nabla^2 I(\boldsymbol{x}, t) = \nabla \cdot \int_A D(\boldsymbol{x} - \boldsymbol{X}) \boldsymbol{n} dA, \tag{12}$$

where $\boldsymbol{X}$ and $\boldsymbol{n}$ are, respectively, the position vector and unit normal vector of a Lagrangian node on the capsule membrane. A is the interfacial area. $D(\boldsymbol{x} - \boldsymbol{X})$ is a smoothed approximation of the Dirac Delta function.[29,32] The Poisson equation [Eq. (12)] is solved by the finite difference method as detailed in Refs. 33 and 34.

C. Validations

The method has been verified extensively for behaviors of a capsule in fluid-structure interaction problems involving viscoelastic fluids.[4,28,32] In addition, further validation of the present method against problems involving complex geometries is provided in the Subsections 1 and 2 of Appendix A.

Here, the effects of the dimensionless diffusion parameter on the behaviors of the capsule are evaluated. To determine a suitable value of the dimensionless diffusion parameter Pr involved in this problem, several simulations are conducted with different values of Pr at $Wi = 1.0$ for N/V flow. Figure 2 shows the evolutions of the lengths of the capsule (length L_x, width L_y, and height L_z, scaled by $2R$) at $L_p^2 = 10^3$, $Wi = 1.0$ and $Pr = 5.0 \times 10^{-3}$, 1.0×10^{-2}, and 2.0×10^{-2}. It is observed that the diffusion parameter Pr does not remarkably affect the deformation of the capsule when Pr is not larger than 1.0×10^{-2}. Therefore, $Pr = 5.0 \times 10^{-3}$ is utilized in the present study.

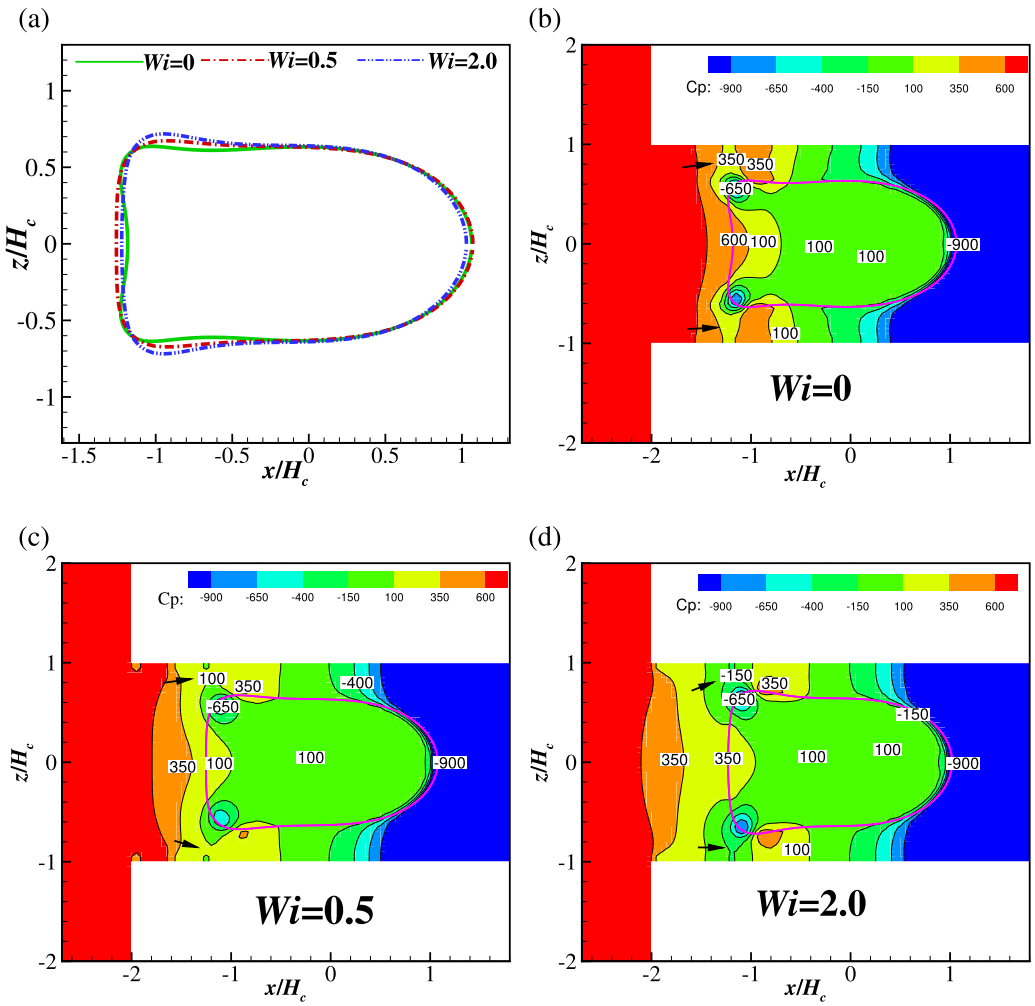

FIG. 7. (a) The instantaneous profiles of the capsule in plane $y = 0$ at $x_c/H_c = -0.226$ and different Wi. (b)–(d) The distributions of the pressure coefficient C_p at different Wi.

III. RESULTS AND DISCUSSION

In this work, simulations are conducted at $Re = 0.5$, $Ca = 0.0333$, $e_b = 0.001$, $Br = 1.0$, $\beta = 0.5$, $Pr = 5 \times 10^{-3}$, and different values of Wi (ranging from 0 to 2.0 for the N/V flow and 0 to 100.0 for the V/N flow), ξ_μ (ranging from 0.2 to 5.0), L_p^2 (ranging from 10 to 10^3 for the N/V flow and 10^{-2} to 10^{10} for the V/N flow) are utilized to evaluate effects of these parameters on the dynamics of the capsule flowing through the channel constriction segment in N/V and V/N flows.

A. A Newtonian capsule in a viscoelastic matrix (N/V flow)

Here, the dynamics of a capsule enclosing a Newtonian fluid in a viscoelastic matrix are examined. The effects of the Weissenberg number Wi, the ratio of the total viscosity ξ_μ and the extensibility parameter of the polymer L_p^2 on the capsule deformation are studied.

1. Effects of Wi

The effects of the Weissenberg number Wi on the capsule dynamics are studied here, and the matched total viscosity ratio $\xi_\mu = 1$ and the extensibility parameter $L_p^2 = 10^3$ are used. Figure 3 shows evolutions of lengths (i.e., length L_x, width L_y, and height L_z, scaled by $2R$) of the capsule as a function of the capsule center position x_c/H_c (in x direction) at different Wi. It is found that all lengths of the capsule experience oscillations when the capsule moves through the channel constriction segment. This is understandable since the capsule experiences changes in its shape (due to the interactions between the capsule and the ambient fluid[16]) when passing through the confinement and expansion structure of the channel (as shown in Fig. 4). In addition, the behaviors of the capsule can be approximately divided into three stages: (I) initial stage ($x_c/H_c < -1.5$), where the capsule is positioned on the left side of the constriction segment, and approaches it; (II) transient stage ($-1.5 < x_c/H_c < 3.5$), where the capsule is inside or just exiting the constriction segment; (III) relaxation stage ($x_c/H_c > 3.5$), where the capsule gradually moves away from

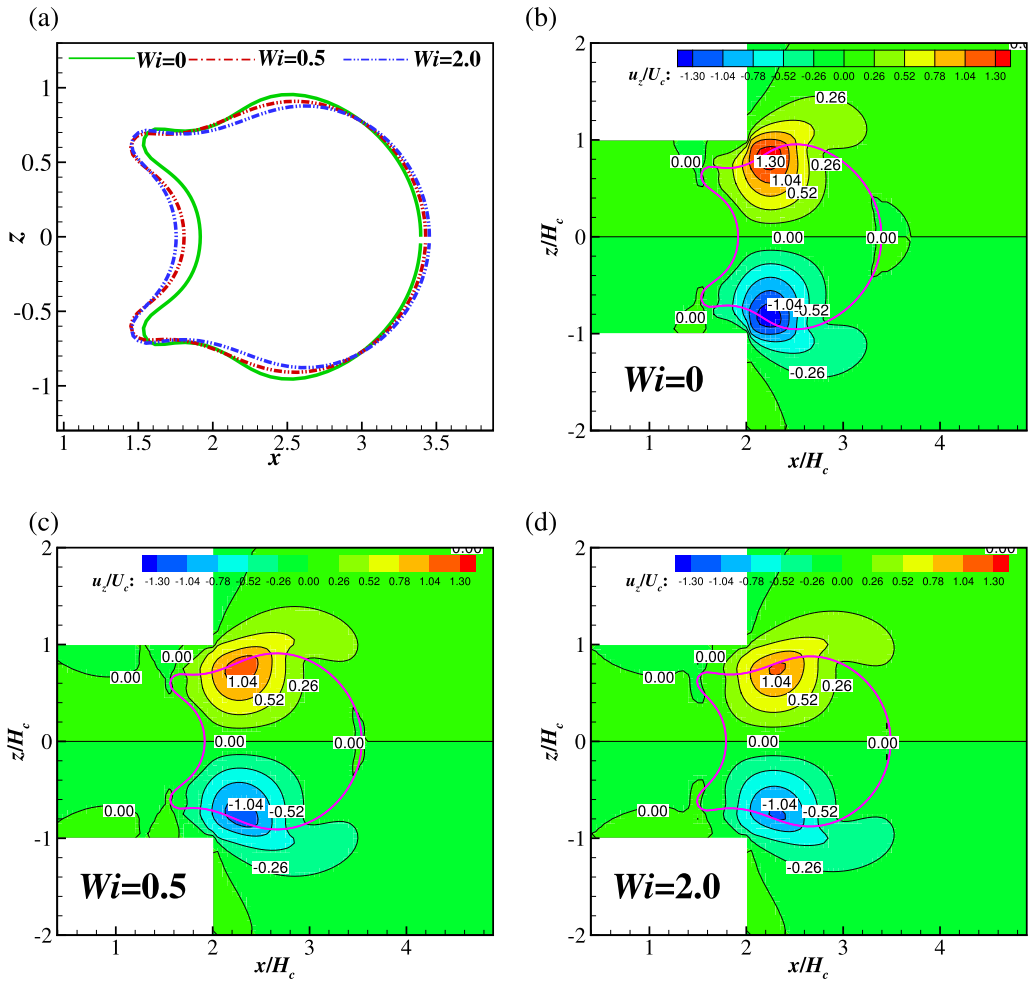

FIG. 8. (a) The instantaneous profiles of the capsule in plane $y = 0$ at $x_c/H_c = 2.375$ and different Wi. (b)–(d) The distributions of the flowing velocity in $z-$ axis direction (u_z) at $x_c/H_c = 2.375$ at different Wi.

the constriction segment. It is found that the Weissenberg number Wi has varying effects on different lengths of the capsule. Specifically, a higher Wi normally leads to a smaller width (L_y) of the capsule in all three stages. In contrast, the effects of Wi on L_x and L_z are different depending on the capsule position. At stage (I), a higher Wi leads to a smaller L_x and a larger L_z of the capsule. To further illustrate the impact of Wi on L_x and L_z during stage (I), Fig. 5(a) presents the instantaneous profiles of the capsule at different Wi and $x_c/H_c = -2.336$ in the plane $y = 0$. It is observed that a lower Wi leads to a more elongated leading tip and a smaller height, and this is primarily due to different pressure field distributions at varying Wi. The contours of the pressure coefficient $C_p = (p - p_c)/(0.5\rho_f U_c^2)$ (p_c denoted the pressure at the capsule's center) are displayed in Figs. 5(b)–5(d). The analysis reveals that the pressure difference across the capsule's leading tip drops with increasing Wi, leading to reduced stretching force. This explains the reduction in length (L_x) at higher Wi values. In addition, the regions of high pressure at the upper and lower sides of the capsule membrane (indicated by black arrows) shrinks as Wi increases, leading to the decreased compressive force. This accounts for the increasing height (L_z) with rising Wi.

During stage (II), the length of the capsule (L_x) experiences continuous decrease as x_c increases, and this reduction is more pronounced at smaller Wi. The decrease in the length L_x is caused by the different flowing velocities at the head and tail of the capsule. Figure 6 shows the distributions of the flowing velocity in $x-$ axis direction (u_x) at $x_c/H_c = -0.226$ for $Wi = 0$, 0.5, and 2.0. It is observed that the flowing velocity at the tail of the capsule surpasses that at the head for all Wi, and this velocity difference contributes to the reduction in the length of the capsule (L_x). In addition, it is also found that the high-velocity region at the tail shrinks as Wi increases, leading to the smaller velocity disparity between the tail and head of the capsule at higher Wi. This explains why L_x experiences a more rapid decline at lower Wi.

The height of the capsule L_z increases with increasing x_c, especially at x_c/H_c larger than 2.0, where the capsule is moving out of the constriction segment. This is because of the expansion in the cross

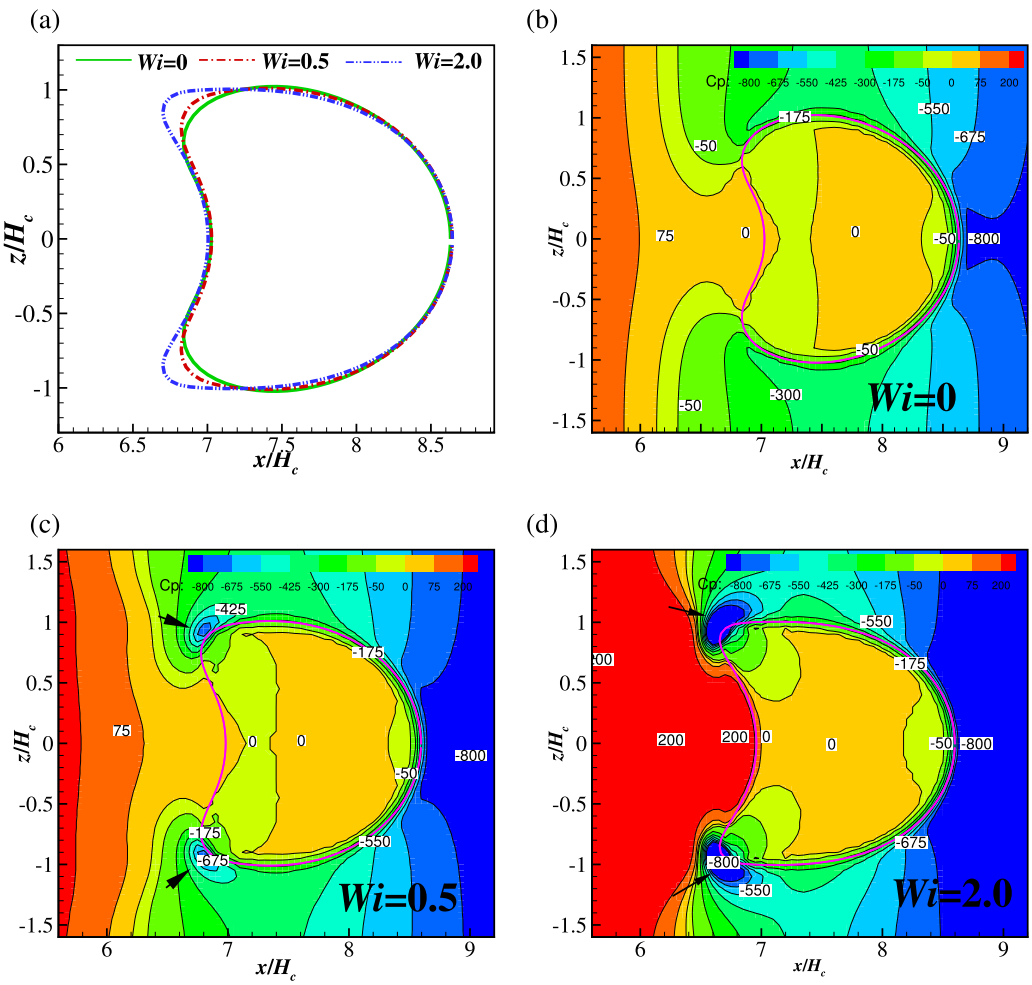

FIG. 9. (a) The instantaneous profiles of the capsule in plane $y = 0$ at $x_c/H_c = 7.579$ and different Wi. (b)-(d) The distributions of the pressure coefficient C_p at different Wi.

section at the right side of the constriction segment.[16] In addition, the viscoelasticity of the external liquid has different effects on L_z depending on the position of the capsule. When x_c/H_c is no larger than 1.5, the height of the capsule L_z is normally larger at higher Wi. In order to further illustrate the influence of Wi on the capsule deformation at $x_c/H_c < 1.5$, the profiles of the capsule in plane $y = 0$ at $Wi = 0$, 0.5, and 2.0 and $x_c/H_c = -0.226$ are shown in Fig. 7(a). It is found that the tail of the capsule is more stretched (in $z-$ axis direction) at higher Wi. This is caused by different pressure distributions at the upper and lower sides of the capsule tail. Figures 7(b)–7(d) illustrate the contours of the pressure coefficient C_p at $x_c/H_c = -0.226$ and $Wi = 0$, 0.5, and 2.0. It is observed that there are two low pressure centers inside capsule tips, and the pressure at the upper and lower sides of the capsule tail (pointed by black arrows) decreases with the increase in Wi leading to lower pressure differences across the upper and lower tips. This means the compressing forces on the capsule tail is smaller at higher Wi, which explains why higher Wi leads to smaller L_z. The effect of Wi on L_z is opposite at $1.5 < x_c/H_c < 3.5$. The profiles of the capsule in plane $y = 0$ at $Wi = 0$, 0.5, and 2.0 and $x_c/H_c = 2.375$ are shown in Fig. 8(a) to illustrate the influence of Wi on the capsule shape. It is observed that the capsule has a larger height at a smaller Wi. This is induced by the larger flowing velocities in the $z-$ axis direction at the right side of the constriction segment at a smaller Wi [as shown in Figs. 8(b)–8(d)].

At stage (III), the capsule completely exits and moves away from the constriction segment, and the shape of the capsule is supposed to relax toward the "bullet" shape when placed in a Newtonian matrix.[16] However, the deformation of the capsule is different when the capsule is exposed to a viscoelastic matrix. It is observed that (from Fig. 3) the height of the capsule (L_z) converges to close values at different Wi, but the length of the capsule (L_x) increases with the increase in Wi. The instantaneous profiles of the capsule in plane $y = 0$ at $Wi = 0$, 0.5, and 2.0 and $x_c/H_c = 7.579$ are shown in Fig. 9(a). An obvious influence of Wi is the elongated tail of the capsule, and it seems that the capsule experiences stronger stretching forces at the upper and lower tips at

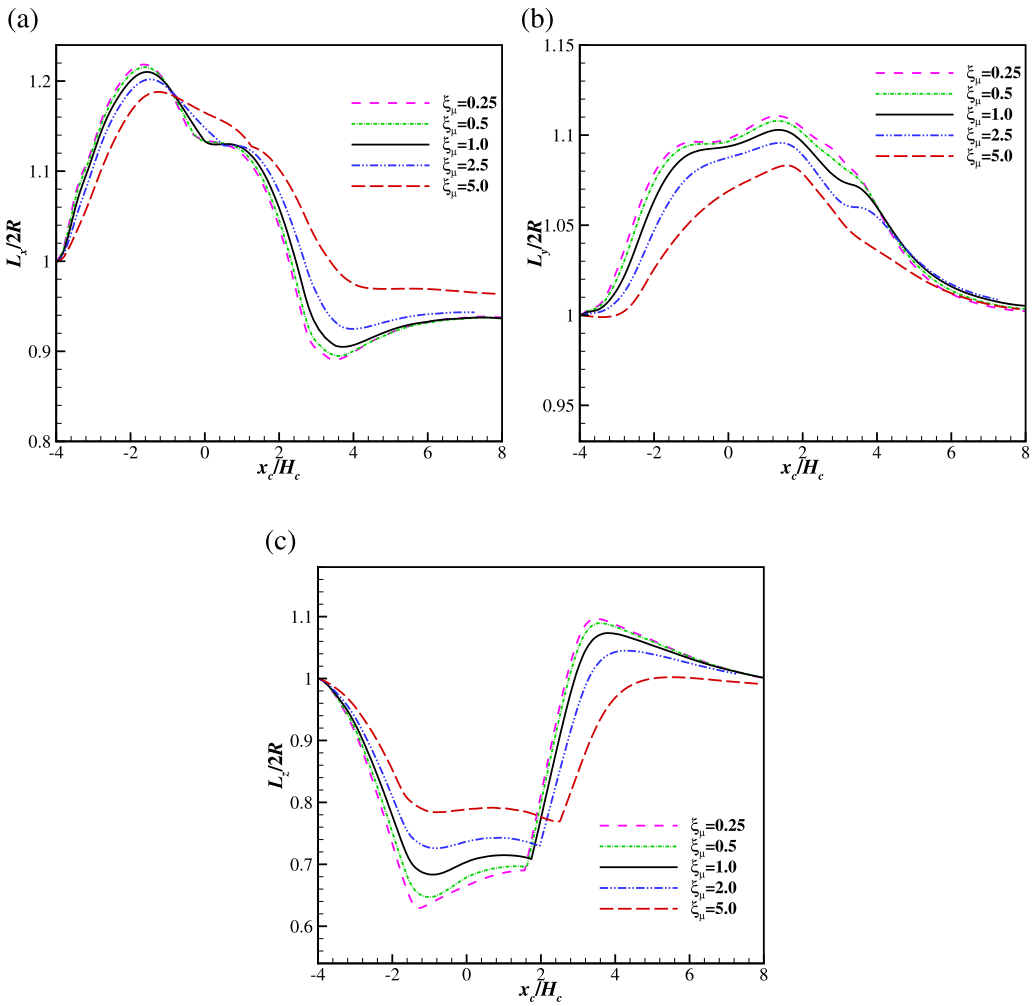

FIG. 10. The evolution of the lengths of the capsule as a function of the position of the capsule center x_c at $Wi = 1.0$ and $L_p^2 = 10^3$ and different ξ_μ. (a) Length L_x, (b) width L_y, and height (c) L_z (scaled by the initial diameter of the capsule $2R$).

higher Wi. To explain the different deformations of the capsule at different Wi, the distributions of the pressure coefficient C_p at $Wi = 0$, 0.5, and 2.0 are, respectively, illustrated in Figs. 9(b)–9(d). It is found that low pressure regions appear (pointed by black arrows) at lower and upper tips of the capsule at $Wi = 0.5$ and 2.0. In addition, the low pressure regions expand with the increase in Wi, accompanied by the decrease in the lowest pressure. This causes larger pressure differences across the tips of the capsule leading to stronger stretching forces at tips of the capsule at higher Wi. In contrast, low pressure regions do not appear at the upper and lower tips of the capsule at $Wi = 0$ [as shown in Fig. 9(b)]. This is why the capsule has larger L_x at higher Wi.

2. Effects of ξ_μ and L_p^2

The effects of the total viscosity ratio ξ_μ and the polymer extensibility parameter L_p^2 on the capsule dynamics are evaluated here. Figure 10 shows the evolutions of the capsule lengths at $Wi = 1.0$, $L_p^2 = 10^3$ and different ξ_μ. It is found that a global effect of ξ_μ is to reduce the magnitude of oscillations of the capsule lengths, which means the inner viscosity tends to hinder the capsule deformation. This trend has also been reported in previous studies on capsule deformation in a shear flow[40] or through a constriction[16] in N/N flows. It has been reported that the deformation of the capsule is governed by the competitive relation of the stresses of internal and external fluids.[16] The external fluid tends to improve the capsule deformation, and the external fluid stresses tend hinder the capsule deformation. Here, the viscous stress of the internal fluid is supposed to increase with increasing ξ_μ with the stresses of outer fluid being the same. This means a higher hindering effect is exerted on the capsule by the inner fluid at higher ξ_μ, and this is why the capsule lengths tend to experience oscillations with deceasing magnitudes with the increase in ξ_μ.

Figure 11 illustrates the effects of the polymer extensibility parameter L_p^2 on the capsule deformation. It is observed that as L_p^2

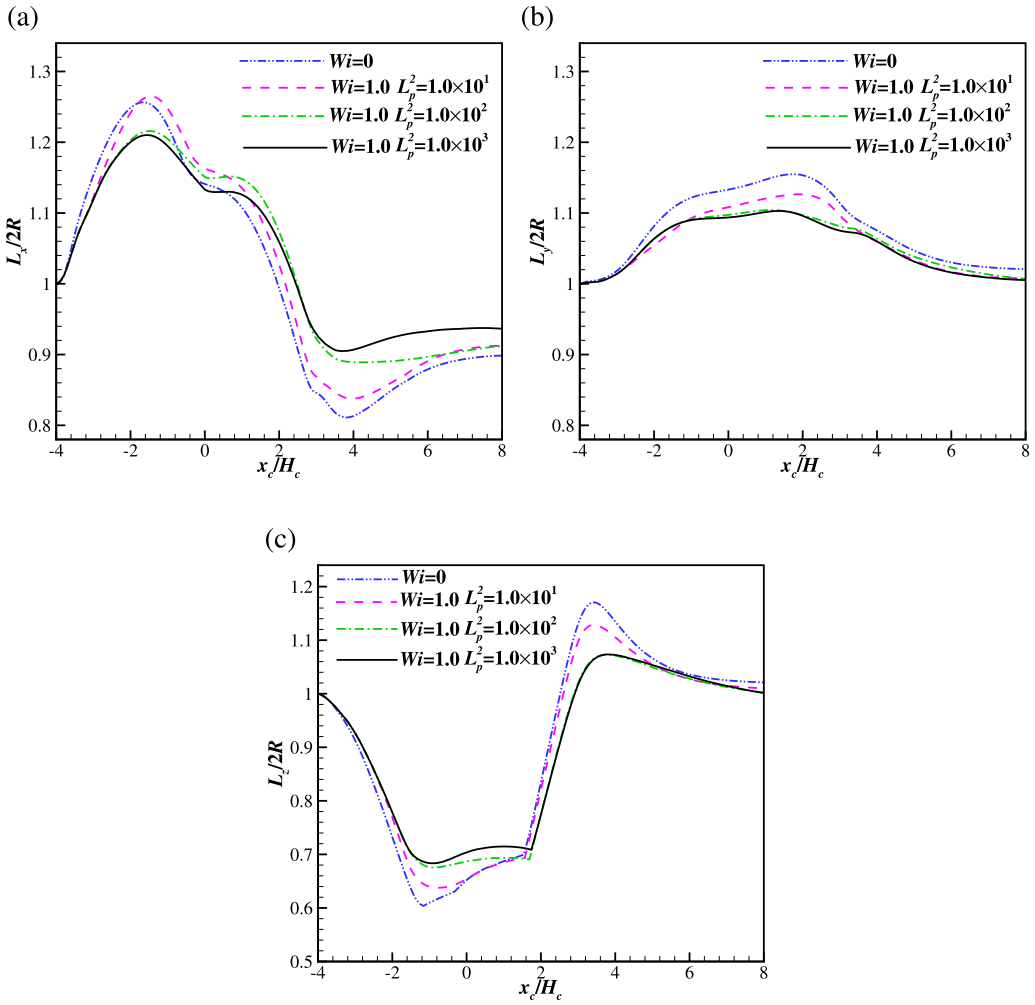

FIG. 11. The evolution of the lengths of the capsule as a function of the position of the capsule center x_c at $Wi = 1.0$ and $\xi_\mu = 1.0$ and different L_p^2. (a) Length L_x, (b) width L_y, and height (c) L_z (scaled by the initial diameter of the capsule $2R$). Please note that the evolutions of capsule lengths in the single-phase Newtonian flow with $\xi_\mu = 1.0$ are drawn (blue lines) for reference.

decreases, the capsule deformation gradually approaches that in a single-phase Newtonian flow with the same total viscosity ratio. This is due to the diminished viscoelastic effect of the fluid at lower L_p^2. The polymer extensibility parameter L_p^2 quantifies the largest extensional length of polymer spring in the fluid, and a smaller L_p^2 means polymer molecules in the fluid can be less extended, leading to the smaller viscoelastic effect.[41] This explains why the capsule deformation tends to converge to that in the single-phase Newtonian flow with the decrease in the extensibility parameter L_p^2.

B. A viscoelastic capsule in a Newtonian matrix (V/N flow)

The transient behaviors of a viscoelastic capsule in a Newtonian matrix are investigated in this section, and effects of the Weissenberg number Wi, the ratio of the total viscosity ξ_μ and the polymer extensibility parameter L_p^2 on the capsule deformation are evaluated.

1. Effects of Wi

The effects of the Weissenberg number Wi on the capsule dynamics are studied here, and the total viscosity ratio $\xi_\mu = 5.0$ and the polymer extensibility parameter $L_p^2 = 1.0 \times 10^3$ are used. Figure 12 shows evolutions of lengths L_x, L_y, and L_z (scaled by $2R$) of the capsule as a function of the capsule center position x_c/H_c at different Wi. It is observed that the behaviors of the capsule can be also divided into three stages: (I) initial stage ($x_c/H_c < -1.5$), (II) transient stage ($-1.5 < x_c/H_c < 4.0$), and (III) relaxation stage ($x_c/H_c > 4.0$). However, the effects of the Weissenberg number Wi on lengths of the capsule are remarkably different from those in the N/V flow. For example, the higher Wi leads to the larger length L_x and the smaller height L_z of the capsule at stage (I), and L_x and L_z, respectively, experiences more rapid decrease and increase at higher Wi at stage (II). These effects are opposite to those in the N/V flow (see Fig. 3 for more details). To further show the effect of Wi on the capsule behaviors, the instantaneous profiles of the capsule at $x_c/H_c = -2.369$, 0.581, 3.0,

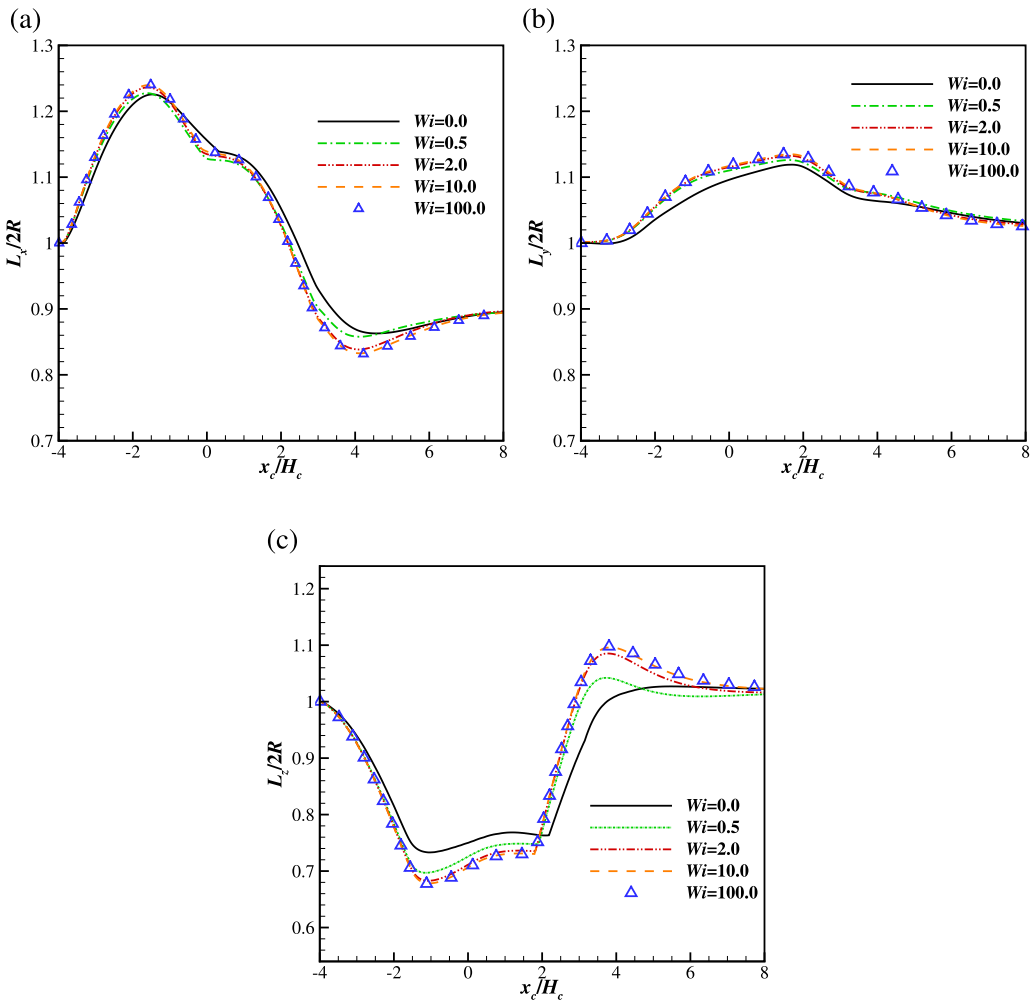

FIG. 12. The evolution of the lengths of the capsule as a function of the position of the capsule center x_c at $\xi_\mu = 1$ and $\beta = 0.5$ and different Wi in the V/N flow. (a) Length L_x, (b) width L_y, and height (c) L_z (scaled by the initial diameter of the capsule $2R$).

and 7.392 at different Wi are illustrated in Fig. 13. It is observed that the capsule tends to have a more elongated leading tip and a smaller height at higher Wi at stage (I), and it is also caused by the different pressure distributions (as shown in Fig. 14). As observed in Fig. 14, the pressure difference across the leading tip of the capsule increases with the increase in Wi, leading to a higher stretching force at higher Wi. That is why the capsule has a larger length (L_x) at larger Wi. In addition, the high pressure regions inside the capsule shrinks at larger Wi, which causes the larger compressing force on the capsule. This is why the capsule experiences a smaller height (L_z) at higher Wi.

At stage (II), the length of the capsule L_x undergoes a continuous decrease similar to the behavior observed in the N/V flow. However, there is a distinct difference in the trend: as the Weissenberg number (Wi) increases, the decrease in L_x becomes more rapid. Regarding the height of the capsule, L_z, it initially demonstrates a gradual increase when $x_c/H_c < 2.0$. Subsequently, in the range of $2.0 < x_c/H_c < 4.0$, there is a rapid rise in L_z. Additionally, higher values of Wi result in a more rapid increase in L_z, especially at $2.0 < x_c/H_c < 4.0$. These trends can be also attributed to the distinct distributions of the pressure and velocity fields, which are similar to those discussed in Sec. III A 1. However, for brevity, the detailed representations of these pressure and velocity distributions are not presented here.

At stage (III), the capsule tends to relax to the same profile at all Wi (same L_x, L_y, and L_z), which is further confirmed by the instantaneous profiles shown in Fig. 13(d). In addition, it has also been observed that the viscoelasticity of the fluid does not significantly impact the behaviors of the capsule as the value of Wi exceeds 2.0. This trend has also been observed for the deformation of a capsule in shear V/N flows,[35] and it is caused by the strong relaxation effect of the viscoelastic fluid.

2. Effects of ξ_μ and L_p^2

In this section, the effects of the total viscosity ratio ξ_μ and the polymer extensibility parameter L_p^2 on the capsule dynamics in the V/N flow are evaluated. Figure 15 shows the evolutions of the capsule

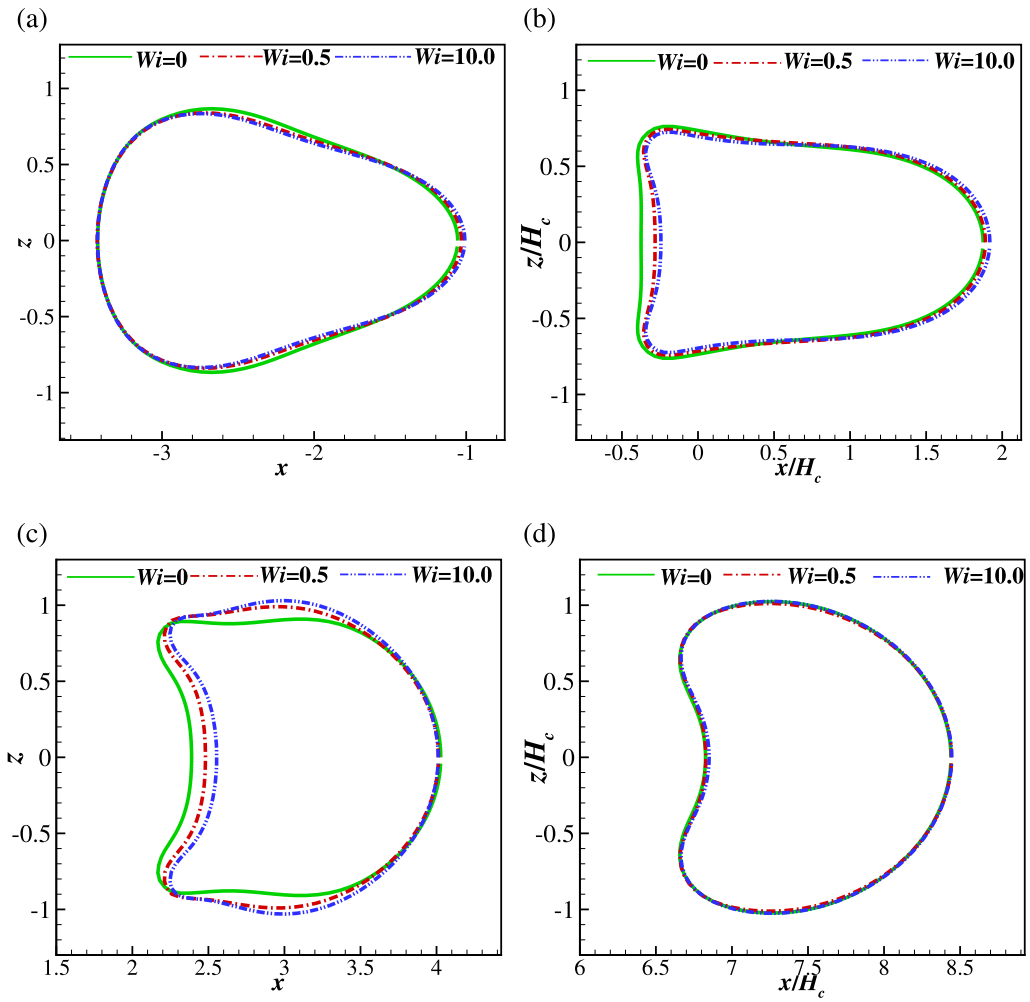

FIG. 13. The instantaneous profiles of the capsule at $\xi_\mu = 5.0$, $L_p^2 = 1.0 \times 10^3$ and different Wi at different positions: (a) $x_c/H_c = -2.369$, (b) $x_c/H_c = 0.581$, (c) $x_c/H_c = 3.0$ and (d) $x_c/H_c = 7.392$.

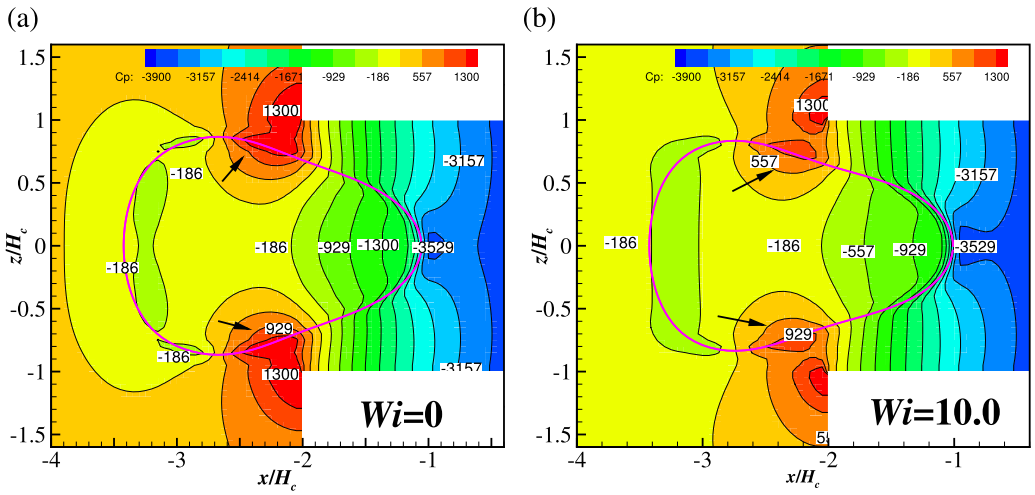

FIG. 14. The distributions of the pressure coefficient C_p at $\xi_\mu = 5.0$, $L_p^2 = 10^3$ and (a) $Wi = 0$ and (b) $Wi = 10.0$.

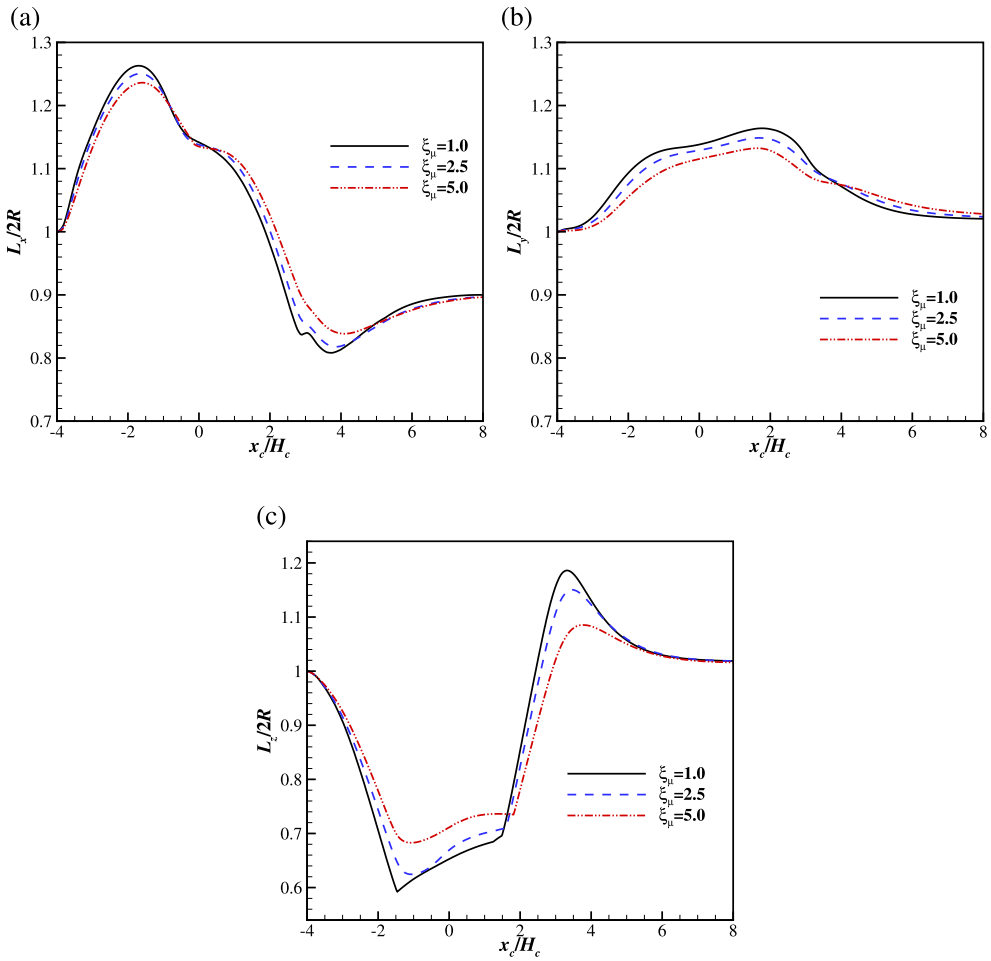

FIG. 15. The evolution of the lengths of the capsule as a function of the position of the capsule center x_c at $Wi = 2.0$ and $L_p^2 = 10^3$ and different ξ_μ. (a) Length L_x, (b) width L_y, and height (c) L_z (scaled by the initial diameter of the capsule $2R$).

lengths at $Wi = 2.0$, $L_p^2 = 10^3$ and different ξ_μ. It is observed that the lengths of the capsule experiences oscillations with smaller amplitudes at higher ξ_μ as found in N/V flow. The effects of the polymer extensibility parameter L_p^2 on the capsule deformation in V/N flow is illustrated in Fig. 16. It is found that L_p^2 does not show remarkable influence on the deformation of the capsule within a wide range of L_P^2 ($1.0 \times 10^{-2} \leq L_p^2 \leq 1.0 \times 10^{10}$).

C. A biconcave capsule passing through the constriction segment

Red blood cells as an essential component of blood may encounter different flow conditions (e.g., vessels with stenosis) when moving in blood vessels. Therefore, it is beneficial to study the behaviors of a red blood cell in a refined channel. Here, the deformation of a red blood cell moving through a microchannel with a constriction is investigated. The geometry for a red blood cell is set as:[42]

$$\begin{aligned} \mathrm{x} &= R_0\eta, \quad y = R_0\zeta, \\ |z| &= 0.5R_0(1-r^2)^{0.5}(0.207 + 2.003r^2 - 1.123r^4), \end{aligned} \tag{13}$$

where $r^2 = \eta^2 + \zeta^2$ and R_0 is a constant used to adjust the volume of the red blood cell.

In this section, the simulations are conducted with the following parameter values: $Re = 0.5$, $Ca = 0.167$, $e_b = 0.001$, $Br = 0.5$, $\beta = 0.5$, $Pr = 5 \times 10^{-3}$, $Wi = 0 - 2.0$, $\xi_\mu = 5.0$, and $L_p^2 = 10^3$. These parameters are defined based on the equivalent radius of the red blood cell, $R = (3V/4\pi)^{1/3}$, where V is the volume of the red blood cell. Initially, the red blood cell is positioned at the center of the microchannel's cross-section at $x = -8H_c$. Figure 17 illustrates the serial profiles of the red blood cell in both V/N and N/V flows at $Wi = 2.0$. It is observed that the red blood cell undergoes shape changes in both cases, and it exhibits a sharper leading tip in the microchannel constriction in the V/N flow compared with that in the N/V flow [as illustrated in Fig. 17(a)]. This observation aligns with the findings in the

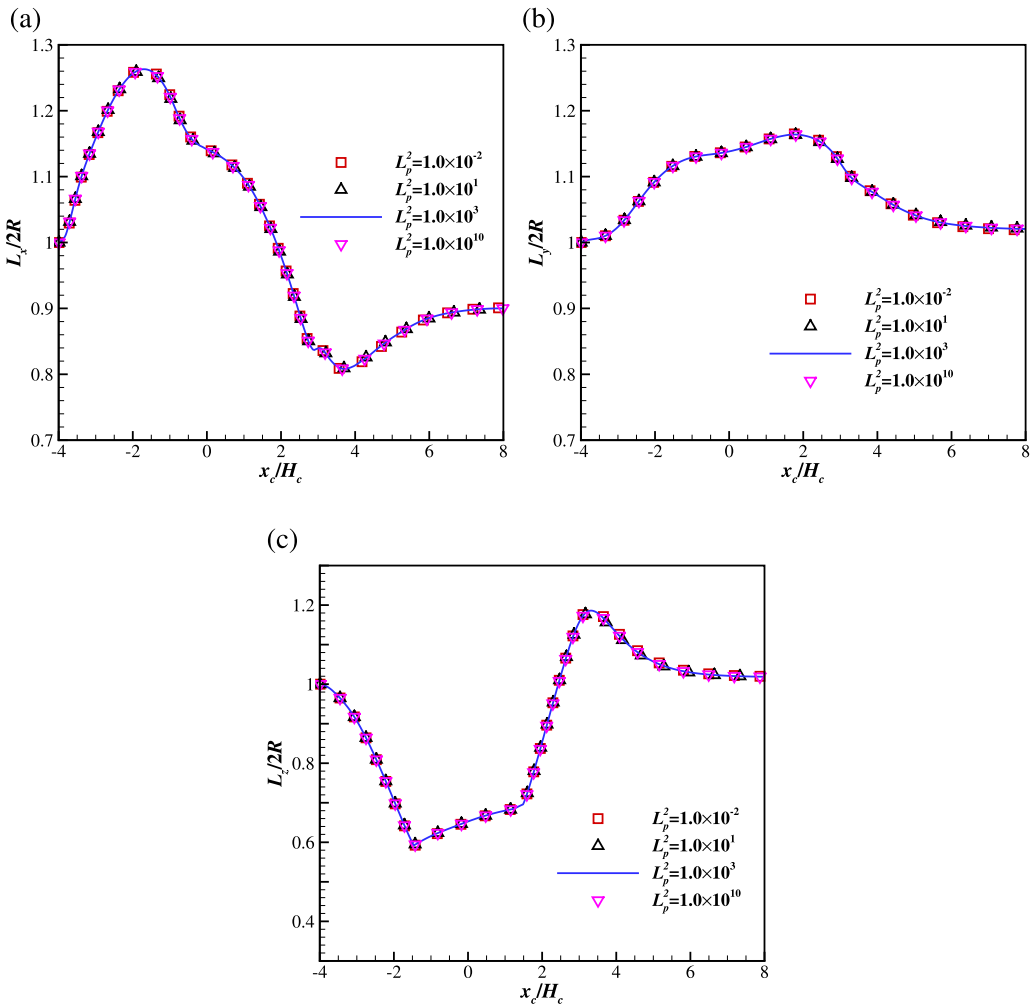

FIG. 16. The evolution of the lengths of the capsule as a function of the position of the capsule center x_c at $Wi = 2.0$, $\xi_\mu = 1.0$ and different L_p^2. (a) Length L_x, (b) width L_y, and height (c) L_z (scaled by the initial diameter of the capsule $2R$).

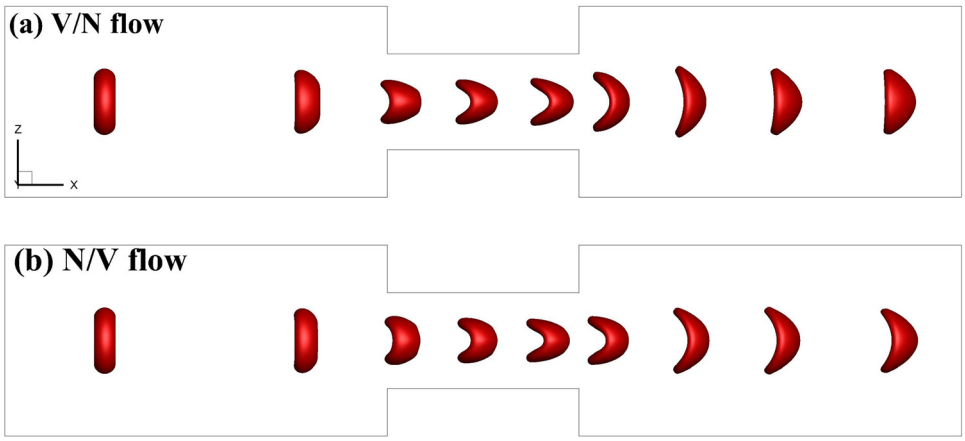

FIG. 17. The serial profiles of the red blood cell through the microchannel constriction at $Wi = 2.0$ in (a) the V/N flow and (b) the N/V flow.

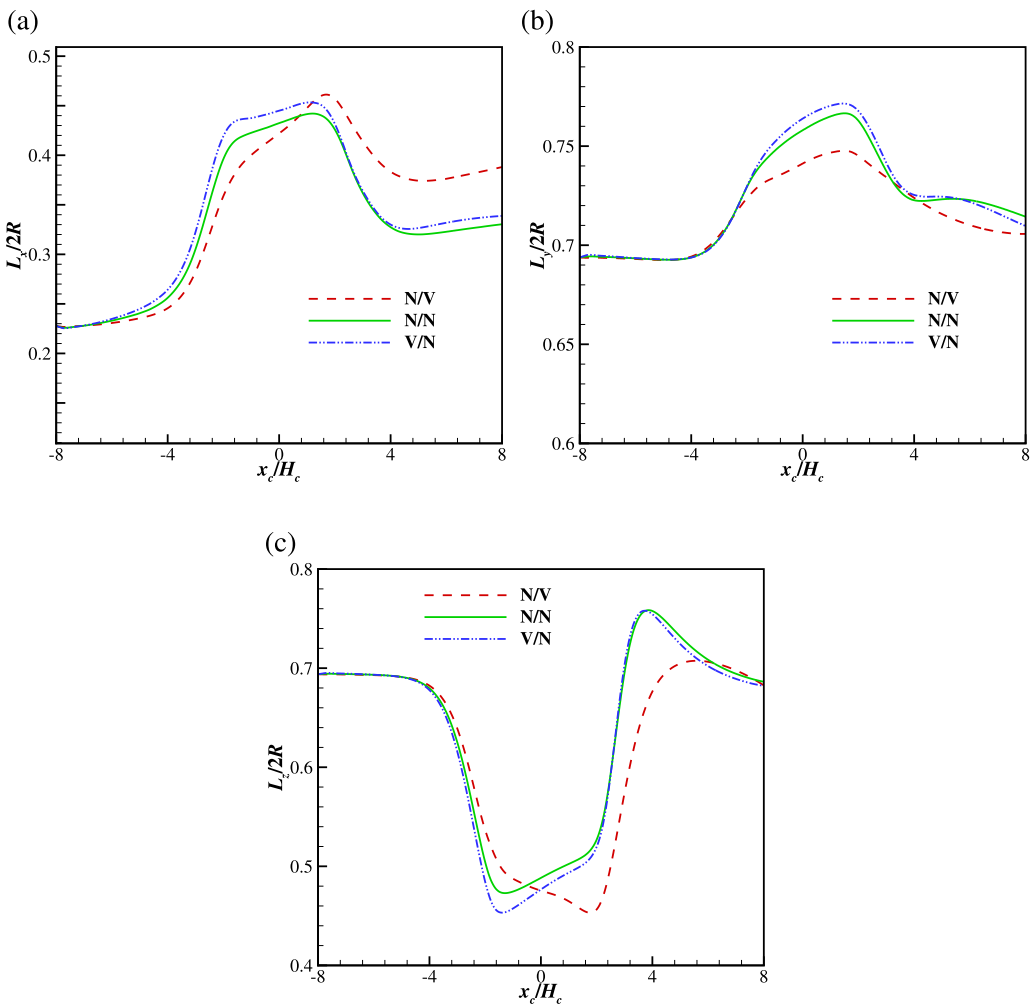

FIG. 18. The evolution of the lengths of the red blood cell in different flows (N/V, N/N and V/N) as a function of the center position x_c at $Wi = 2.0$ and $L_p^2 = 10^3$ and $\xi_\mu = 5.0$. (a) Length L_x, (b) width L_y, and height (c) L_z (scaled by the initial equivalent diameter of the red blood cell $2R$).

spherical capsule cases (Secs. III A and III B). Furthermore, in the V/N flow, the red blood cell tends to relax into a "parachute" shape, while in the N/V flow, it adopts a "sickle" shape.

To provide further insight into the behavior of red blood cells, Fig. 18 presents the evolutions of the lengths L_x, L_y, and L_z (scaled by $2R$) as a function of the capsule center position x_c/H_c in V/N, N/N, and N/V flows at $Wi = 2.0$. It can be observed that the lengths of the red blood cell exhibit similar trends in V/N, N/N, and N/V flows before entering the constriction segment. However, distinct variations are observed as the red blood cell passes through the constriction segment. Specifically, the length of the red blood cell (L_x) increases more rapidly in the N/V flow compared to N/N and V/N flows. Additionally, the height of the red blood cell (L_z) undergoes a decline rather than a continuous increase in N/N and V/N flows. After exiting the constriction segment, the red blood cell tends to exhibit a larger length (L_x) in the N/V flow compared with N/N and V/N flows, while the height (L_z) gradually relaxes to similar values in all cases. Additionally, the impact of the Weissenberg number on the deformation of the red blood cell as it traverses the constriction segment is further explored. In Fig. 19, the evolution of capsule lengths at different Wi values in the V/N flow is depicted. It reveals that the viscoelastic properties of the inner fluid exert a subtle influence on capsule deformation, manifesting as a marginal increase in L_x and a decrease in L_z at the constriction segment. Figure 20 provides the insight into the evolution of capsule lengths at different Wi in the N/V flow. Notably, the viscoelasticity of the external fluid leads to a pronounced enhancement of L_x at higher Wi. This pattern aligns with the observations made in spherical capsule cases.

IV. CONCLUSIONS

In this work, the effects of the fluid rheology on the behaviors of a spherical capsule passing through a microchannel constriction

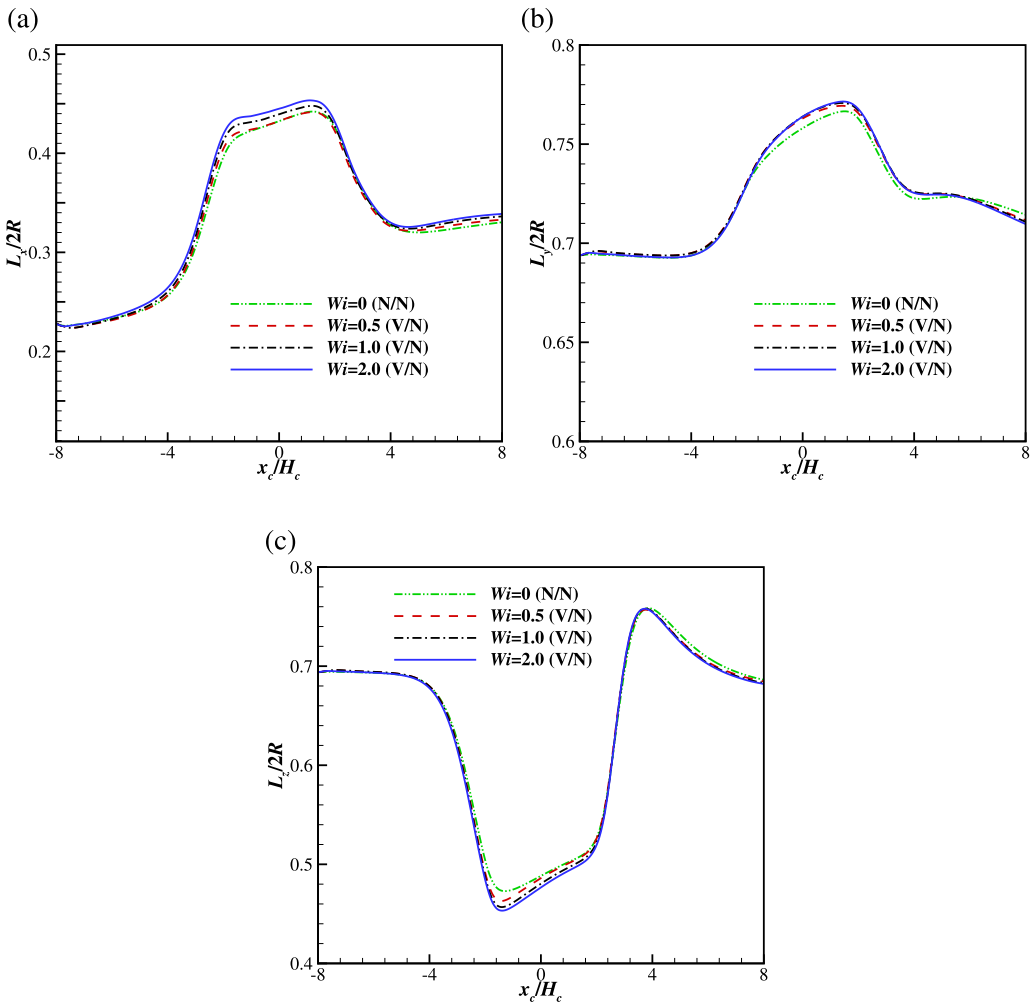

FIG. 19. The evolution of the lengths of the red blood cell as a function of the center position x_c at $L_p^2 = 10^3$, $\xi_\mu = 5.0$ and different Wi in the V/N flow. (a) Length L_x, (b) width L_y, and height (c) L_z (scaled by the initial equivalent diameter of the red blood cell $2R$).

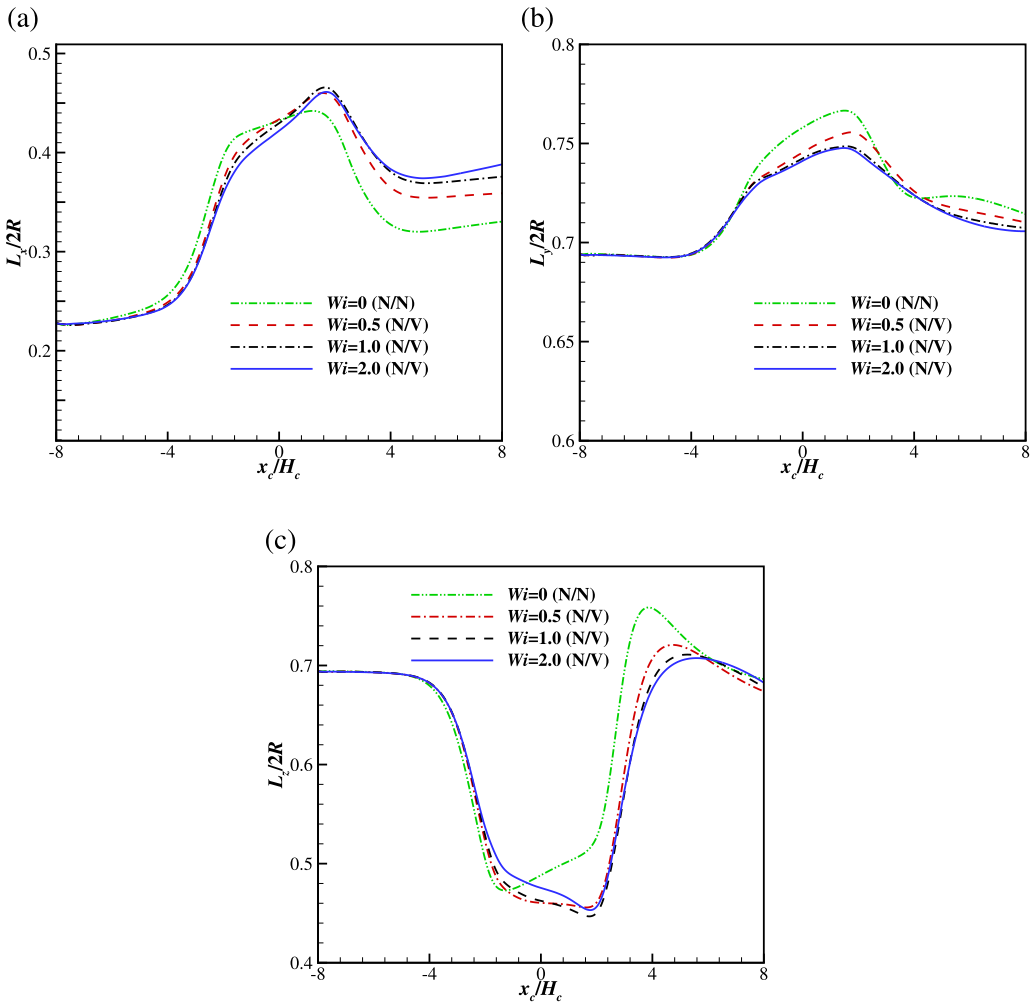

FIG. 20. The evolution of the lengths of the red blood cell as a function of the center position x_c at $L_p^2 = 10^3$, $\xi_\mu = 5.0$ and different *Wi* in the N/V flow. (a) Length L_x, (b) width L_y, and height (c) L_z (scaled by the initial equivalent diameter of the red blood cell $2R$).

are numerically investigated, and the deformation of the capsule in various types of multiphase flows (N/V, N/N, and V/N) is examined. The findings reveal that the lengths of the capsule (length L_x, width L_y, and height L_z) undergo oscillations as the capsule passes through the constriction segment, and their evolutions can be classified into three stages. Initially, as the capsule approaches the constriction segment, the length L_x increases, while the height L_z decreases, with the increase in the capsule center position (x_c/H_c). The viscoelasticity of the fluid exerts different effects on the capsule's lengths in different flow types. In N/V flow, the capsule tends to have a smaller length and a larger height, whereas in V/N flow, the tendency is reversed. These differences arise due to the different pressure field distributions induced by the viscoelastic property of the fluid. During the transient stage, when the capsule is inside or just exiting the constriction segment, L_x generally exhibits a continuous decrease, whereas L_z typically shows an increase. In N/V flow, the length L_x and the height L_z of the capsule show a less rapid decrease and increase, respectively, at higher *Wi*, which is opposite in V/N flow. As the capsule moves away from the microchannel constriction, during the relaxation stage, it tends to adopt similar profiles in V/N and N/V flows while displaying elongated tails in N/V flow. In addition, the red blood cell also experiences changes in its shape during the passage through the microchannel constriction, with a sharper leading tip within the constriction segment in the V/N flow, and it relaxes to different shapes in V/N and N/V flows (the parachute shape in the V/N flow and the sickle shape in the N/V flow).

ACKNOWLEDGMENTS

This work is supported by the National Natural Science Foundation of China (Grant No. 82172066), the Beijing Municipal Natural Science Foundation (Grant No. Z190014), and the Australian Research Council (Grant No. DE160101098).

AUTHOR DECLARATIONS

Conflict of Interest

The authors have no conflicts to disclose.

Author Contributions

Jingtao Ma: Formal analysis (equal); Investigation (lead); Resources (equal); Validation (equal); Visualization (lead); Writing – original draft (lead). **Qiuxiang Huang:** Data curation (equal); Formal analysis (equal); Software (equal); Validation (equal); Visualization (equal). **Yi Zhu:** Data curation (supporting); Formal analysis (equal); Resources (equal); Writing – review & editing (supporting). **Yuan-Qing Xu:** Conceptualization (equal); Funding acquisition (equal); Investigation (equal); Supervision (equal); Visualization (equal); Writing – review & editing (equal). **Fang-Bao Tian:** Conceptualization (equal); Funding acquisition (supporting); Investigation (equal); Resources (supporting); Supervision (equal).

DATA AVAILABILITY

The data that support the findings of this study are available from the corresponding author upon reasonable request.

APPENDIX A: VALIDATIONS OF THE NUMERICAL METHOD

1. A Newtonian spherical capsule flowing through a constriction in a microchannel filled with a Newtonian fluid

Here, the deformation of an initially spherical capsule enclosing a Newtonian fluid through a constriction in a microchannel filled with a Newtonian fluid is considered to validate the present method. The geometry of the microchannel is shown in Fig. 1. A fully developed Poiseuille flow with the averaged velocity U_c is applied to the inlet of the microchannel (left boundary), the

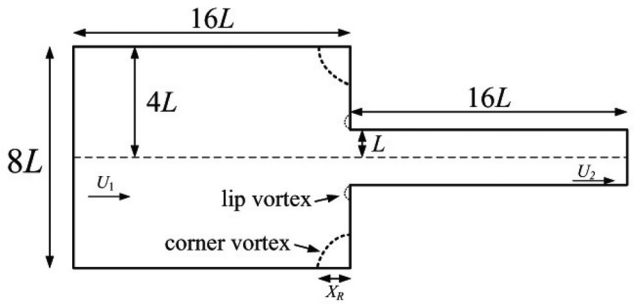

FIG. 22. Schematic diagram of the planar 4:1 contraction flow.

Neumann boundary condition ($\partial \boldsymbol{u}/\partial x = 0$) is given at the outflow boundary (right boundary), and other boundaries are treated as solid walls. The capsule (with an initial radius R) modeled by the Skalak's law (with $C = E_a/E_s = 1$) is initially placed at center of the cross-section of the microchannel and $x = -4H_c$, and a prestress $\alpha_p = 0.05$ is enforced to the capsule to be consistent with the study by Park and Dimitrakopoulos[16] (Please refer to Park and Dimitrakopoulos[16] for more details about the prestress). Following the configuration by Ref. 16, the capillary number $Ca = \mu_s^{out} U_c/E_s = 0.0333$ and the non-dimensional bending stiffness $e_b = E_b/(E_s R^2) = 0$ are used here. Simulations are performed for different viscosity ratios $\xi_\mu = \mu_s^{in}/\mu_s^{out} = 1.0$ and 5.0. The Reynolds number is $Re = \rho_f^{out} U_c W/\mu_s^{out} = 0.25$, and the blockage ratio at the contraction segment is $Br = 2R/2H_c = 0.9$.

The grid spacing used is $\Delta x = \Delta y = \Delta z = W/80$, which is sufficient to reach the independence of the mesh size for this problem.[43] Figure 21 shows the evolution of the lengths of the capsule (length L_x, width L_y, and height L_z, normalized with $2R$) with the capsule center position x_c (in x-axis direction), and the present results are compared with the results from Park and Dimitrakopoulos.[16] It is found the present results show very good agreement with those of the previous study.

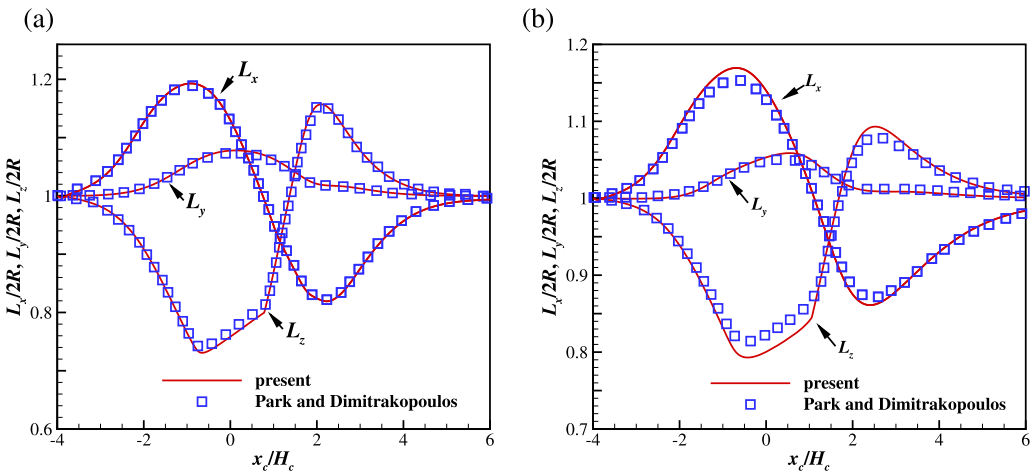

FIG. 21. The evolution of the lengths of the capsule as a function of the position of the capsule center at $Ca = 0.0333$ and $\xi =$ (a) 1.0 and (b) 5.0. Here, x_c is the position of the capsule center in the $x-$ axis direction.

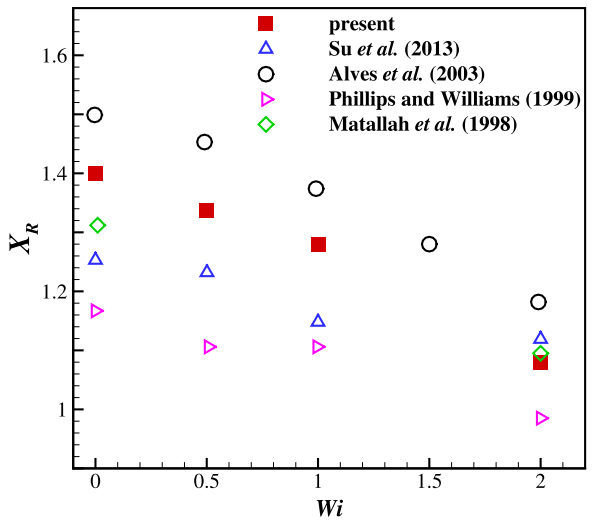

FIG. 23. The evolution of the salient vortex length X_R as a function of the Weissenberg number *Wi*.

2. The flow of an Oldroyd-B fluid through the 4:1 planar contraction

The flow of a viscoelastic fluid through a contraction geometry exhibits some critical and intricate characteristics, which makes it a benchmark problem for validations of numerical method involving complex geometries. Here, the flow of an Oldroyd-B fluid through a 4:1 planar contraction is investigated to further validation the present method in problems involving complex geometries. The schematic diagram for this problem is illustrated in Fig. 22. The fully developed Poiseuille flow (with the average velocity U_1) is imposed at the inlet and the Neumann boundary condition is applied at the outlet. The non-slip boundary conditions are used at upper and lower walls. Here, the Reynolds number used is the Reynolds number $Re = \rho_f U_1 W/\mu_0 = 0.067$, the Weissenberg number is defined as $Wi = \lambda_p U_2/L$ with U_2 being the downstream average velocity, the non-dimensional diffusion parameter used is $Pr = \kappa/(U_1 W) = 5 \times 10^{-3}$, and the ratio of the solvent to the total viscosity is $\beta = \mu_s/\mu_0 = 1/9$. Here, $Wi = 0, 0.5, 1.0$ and 2.0 are considered. Following the study by Su *et al.*,[44] the grid spacing $\Delta x = \Delta y = L/80$ is utilized in the simulations. Figure 23 illustrates the evolution of the salient vortex length X_R as a function of the Weissenberg

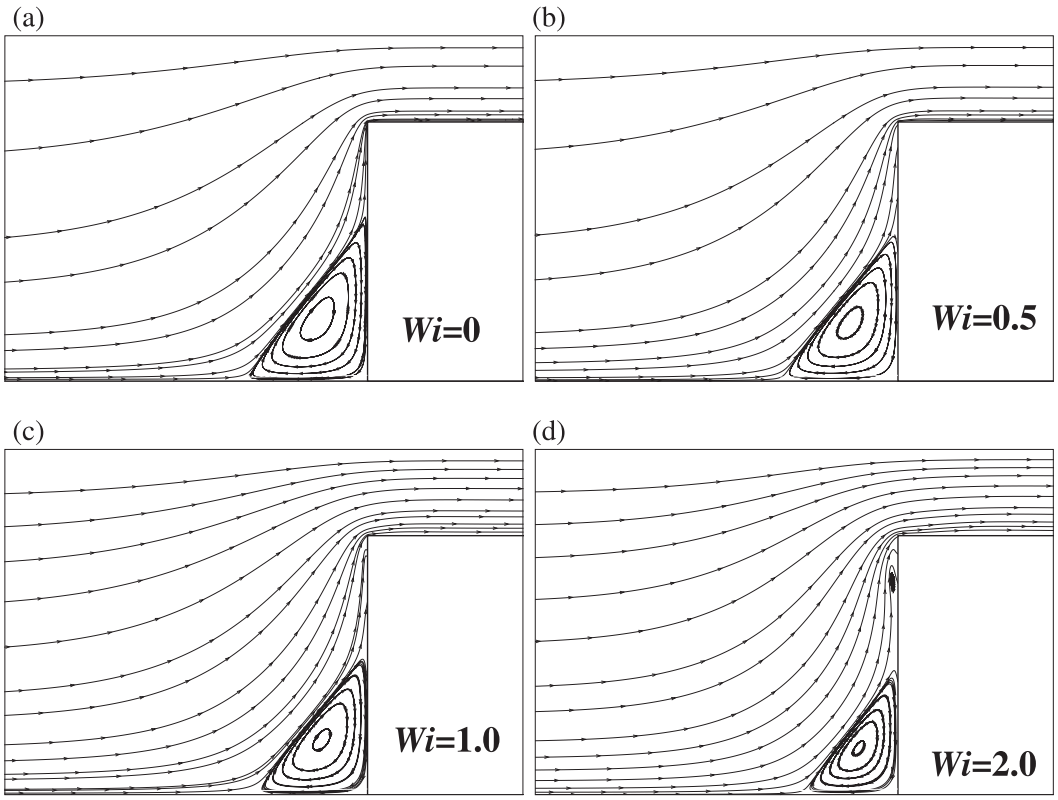

FIG. 24. Flow patterns of the Oldroyd-B fluid at: (a) $Wi = 0$, (b) $Wi = 0.5$, (c) $Wi = 1.0$, and (d) $Wi = 2.0$.

number Wi. It is found that the salient vortex length X_R decreases with increasing Wi, and the present results show good agreement with the previous numerical data in Refs. 44–47. Figure 24 illustrates the flow patterns of the Oldroyd-B fluid at four different Wi ($Wi = 0, 0.5, 1.0$ and 2.0). It has been observed that the lip vortex emerges and grows as Wi is increased, but it is discernible until Wi reaches 2.0. These findings are consistent with Refs. 44 and 47.

REFERENCES

[1]T. Lian and R. J. Ho, "Trends and developments in liposome drug delivery systems," J. Pharm. Sci. **90**, 667–680 (2001).
[2]S. Selvamuthukumar and R. Velmurugan, "Nanostructured lipid carriers: A potential drug carrier for cancer chemotherapy," Lipids Health Dis. **11**, 159 (2012).
[3]S. Wang, J. Gao, and Z. Wang, "Outer membrane vesicles for vaccination and targeted drug delivery," Wiley Interdiscip. Rev.: Nanomed. Nanobiotechnol. **11**, e1523 (2019).
[4]J. Ma, L. Xu, F.-B. Tian, J. Young, and J. C. Lai, "Dynamic characteristics of a deformable capsule in a simple shear flow," Phys. Rev. E **99**, 023101 (2019).
[5]M. Kraus, W. Wintz, U. Seifert, and R. Lipowsky, "Fluid vesicles in shear flow," Phys. Rev. Lett. **77**, 3685 (1996).
[6]J. Mauer, S. Mendez, L. Lanotte, F. Nicoud, M. Abkarian, G. Gompper, and D. A. Fedosov, "Flow-induced transitions of red blood cell shapes under shear," Phys. Rev. Lett. **121**, 118103 (2018).
[7]Z. Wang, Y. Sui, A.-V. Salsac, D. Barthès-Biesel, and W. Wang, "Path selection of a spherical capsule in a microfluidic branched channel: Towards the design of an enrichment device," J. Fluid Mech. **849**, 136–162 (2018).
[8]X.-Q. Hu, A.-V. Salsac, and D. Barthès-Biesel, "Flow of a spherical capsule in a pore with circular or square cross-section," J. Fluid Mech. **705**, 176–194 (2012).
[9]D.-K. Sun, Y. Wang, A.-P. Dong, and B.-D. Sun, "A three-dimensional quantitative study on the hydrodynamic focusing of particles with the immersed boundary–lattice Boltzmann method," Int. J. Heat Mass Transfer **94**, 306–315 (2016).
[10]C. Rorai, A. Touchard, L. Zhu, and L. Brandt, "Motion of an elastic capsule in a constricted microchannel," Eur. Phys. J. E **38**, 49 (2015).
[11]Z. Zhang, J. Xu, and C. Drapaca, "Particle squeezing in narrow confinements," Microfluid. Nanofluid. **22**, 120 (2018).
[12]H. Bow, I. V. Pivkin, M. Diez-Silva, S. J. Goldfless, M. Dao, J. C. Niles, S. Suresh, and J. Han, "A microfabricated deformability-based flow cytometer with application to malaria," Lab Chip **11**, 1065–1073 (2011).
[13]M. G. Lee, J. H. Shin, C. Y. Bae, S. Choi, and J.-K. Park, "Label-free cancer cell separation from human whole blood using inertial microfluidics at low shear stress," Anal. Chem. **85**, 6213–6218 (2013).
[14]Y. Luo, D. Chen, Y. Zhao, C. Wei, X. Zhao, W. Yue, R. Long, J. Wang, and J. Chen, "A constriction channel based microfluidic system enabling continuous characterization of cellular instantaneous Young's modulus," Sens. Actuators, B **202**, 1183–1189 (2014).
[15]R. Kusters, T. van der Heijden, B. Kaoui, J. Harting, and C. Storm, "Forced transport of deformable containers through narrow constrictions," Phys. Rev. E **90**, 033006 (2014).
[16]S.-Y. Park and P. Dimitrakopoulos, "Transient dynamics of an elastic capsule in a microfluidic constriction," Soft Matter **9**, 8844–8855 (2013).
[17]H. Lu and Z. Peng, "Boundary integral simulations of a red blood cell squeezing through a submicron slit under prescribed inlet and outlet pressures," Phys. Fluids **31**, 031902 (2019).
[18]M. Brust, C. Schaefer, R. Doerr, L. Pan, M. Garcia, P. Arratia, and C. Wagner, "Rheology of human blood plasma: Viscoelastic versus Newtonian behavior," Phys. Rev. Lett. **110**, 078305 (2013).
[19]S. Varchanis, Y. Dimakopoulos, C. Wagner, and J. Tsamopoulos, "How viscoelastic is human blood plasma?," Soft Matter **14**, 4238–4251 (2018).
[20]J. Najafi, S. Dmitrieff, and N. Minc, "Size-and position-dependent cytoplasm viscoelasticity through hydrodynamic interactions with the cell surface," Proc. Natl. Acad. Sci. U. S. A. **120**, e2216839120 (2023).
[21]G. Guigas, C. Kalla, and M. Weiss, "Probing the nanoscale viscoelasticity of intracellular fluids in living cells," Biophys. J. **93**, 316–323 (2007).
[22]J. Remmelgas and L. G. Leal, "Computational studies of the FENE-CR model in a two-roll mill," J. Non-Newtonian Fluid Mech. **89**, 231–249 (2000).
[23]W. Helfrich, "Elastic properties of lipid bilayers: Theory and possible experiments," Z. Naturforsch. C **28**, 693–703 (1973).
[24]Z.-C. Ou-Yang and W. Helfrich, "Bending energy of vesicle membranes: General expressions for the first, second, and third variation of the shape energy and applications to spheres and cylinders," Phys. Rev. A **39**, 5280 (1989).
[25]A. Guckenberger, M. P. Schraml, P. G. Chen, M. Leonetti, and S. Gekle, "On the bending algorithms for soft objects in flows," Comput. Phys. Commun. **207**, 1–23 (2016).
[26]Z. Wang, Y. Sui, A.-V. Salsac, D. Barthès-Biesel, and W. Wang, "Motion of a spherical capsule in branched tube flow with finite inertia," J. Fluid Mech. **806**, 603–626 (2016).
[27]R. Skalak, A. Tozeren, R. Zarda, and S. Chien, "Strain energy function of red blood cell membranes," Biophys. J. **13**, 245–264 (1973).
[28]J. Ma, F.-B. Tian, J. Young, and J. C. Lai, "Dynamic behaviours of a filament in a viscoelastic uniform flow," Fluids **6**, 90 (2021).
[29]F.-B. Tian, H. Dai, H. Luo, J. F. Doyle, and B. Rousseau, "Fluid–structure interaction involving large deformations: 3D simulations and applications to biological systems," J. Comput. Phys. **258**, 451–469 (2014).
[30]O. Malaspinas, N. Fiétier, and M. Deville, "Lattice Boltzmann method for the simulation of viscoelastic fluid flows," J. Non-Newtonian Fluid Mech. **165**, 1637–1653 (2010).
[31]N. Goyal and J. Derksen, "Direct simulations of spherical particles sedimenting in viscoelastic fluids," J. Non-Newtonian Fluid Mech. **183–184**, 1–13 (2012).
[32]J. Ma, Z. Wang, J. Young, J. C. Lai, Y. Sui, and F.-B. Tian, "An immersed boundary-lattice Boltzmann method for fluid-structure interaction problems involving viscoelastic fluids and complex geometries," J. Comput. Phys. **415**, 109487 (2020).
[33]G. Tryggvason, B. Bunner, A. Esmaeeli, D. Juric, N. Al-Rawahi, W. Tauber, J. Han, S. Nas, and Y.-J. Jan, "A front-tracking method for the computations of multiphase flow," J. Comput. Phys. **169**, 708–759 (2001).
[34]S. O. Unverdi and G. Tryggvason, "A front-tracking method for viscous, incompressible, multi-fluid flows," J. Comput. Phys. **100**, 25–37 (1992).
[35]Z. Y. Luo and B. F. Bai, "Dynamics of capsules enclosing viscoelastic fluid in simple shear flow," J. Fluid Mech. **840**, 656–687 (2018).
[36]Q. Huang, F.-B. Tian, J. Young, and J. C. Lai, "Transition to chaos in a two-sided collapsible channel flow," J. Fluid Mech. **926**, A15 (2021).
[37]Y. Zhu, F.-B. Tian, J. Young, J. C. Liao, and J. Lai, "A numerical study of fish adaption behaviors in complex environments with a deep reinforcement learning and immersed boundary–lattice Boltzmann method," Sci. Rep. **11**, 1691 (2021).
[38]D.-C. Xu, X.-Y. Tang, A. Li, J.-T. Ma, and Y.-Q. Xu, "External force attached binding focus of particles and its application," Phys. Fluids **35**, 012016 (2023).
[39]F.-B. Tian, H. Luo, L. Zhu, J. C. Liao, and X.-Y. Lu, "An efficient immersed boundary-lattice Boltzmann method for the hydrodynamic interaction of elastic filaments," J. Comput. Phys. **230**, 7266–7283 (2011b).
[40]S. Ramanujan and C. Pozrikidis, "Deformation of liquid capsules enclosed by elastic membranes in simple shear flow: Large deformations and the effect of fluid viscosities," J. Fluid Mech. **361**, 117–143 (1998).
[41]D. Izbassarov and M. Muradoglu, "A computational study of two-phase viscoelastic systems in a capillary tube with a sudden contraction/expansion," Phys. Fluids **28**, 012110 (2016).
[42]Y. Sui, Y. T. Chew, P. Roy, and H. Low, "A hybrid method to study flow-induced deformation of three-dimensional capsules," J. Comput. Phys. **227**, 6351–6371 (2008).
[43]P. Balogh and P. Bagchi, "A computational approach to modeling cellular-scale blood flow in complex geometry," J. Comput. Phys. **334**, 280–307 (2017).
[44]J. Su, J. Ouyang, X. Wang, and B. Yang, "Lattice Boltzmann method coupled with the Oldroyd-B constitutive model for a viscoelastic fluid," Phys. Rev. E **88**, 053304 (2013).
[45]M. A. Alves, P. J. Oliveira, and F. T. Pinho, "Benchmark solutions for the flow of Oldroyd-B and PTT fluids in planar contractions," J. Non-Newtonian Fluid Mech. **110**, 45–75 (2003).
[46]T. Phillips and A. Williams, "Viscoelastic flow through a planar contraction using a semi-Lagrangian finite volume method," J. Non-Newtonian Fluid Mech. **87**, 215–246 (1999).
[47]H. Matallah, P. Townsend, and M. Webster, "Recovery and stress-splitting schemes for viscoelastic flows," J. Non-Newtonian Fluid Mech. **75**, 139–166 (1998).